IEEE Access
Multidisciplinary | Rapid Review | Open Access Journal

Received 15 October 2024, accepted 25 November 2024, date of publication 27 November 2024,
date of current version 9 December 2024.

Digital Object Identifier 10.1109/ACCESS.2024.3507365

RESEARCH ARTICLE

A Novel Method for Estimating Heart Rate Variability Through a Multiple-Input Multiple-Output FMCW Radar

ELIA VIGNOLI[1], (Graduate Student Member, IEEE), GIORGIO GUERZONI[1], AND GIORGIO MATTEO VITETTA[1,2], (Senior Member, IEEE)
[1]Department of Engineering "Enzo Ferrari," University of Modena and Reggio Emilia, 41124 Modena, Italy
[2]Consorzio Nazionale Interuniversitario per le Telecomunicazioni, 43124 Parma, Italy

Corresponding author: Elia Vignoli (elia.vignoli@unimore.it)

ABSTRACT In this manuscript, the problem of assessing the *heart rate variability* (HRV) of a single subject using a colocated multiple-input multiple-output radar of frequency modulated continuous wave type is investigated. The proposed solution exploits beamforming to acquire multiple measurements from different points on the body of the monitored subject. These measurements are combined using a selection strategy that aims at reducing the impact of random body movements while enhancing the overall signal-to-noise ratio. The resulting signal is then filtered using a physiology-inspired filter. Our results demonstrate that the proposed estimation method can accurately identify the instants at which heartbeats occur and achieve accuracy similar to a regular electrocardiogram in terms of specific HRV metrics referring to interbeat intervals.

INDEX TERMS Biomedical engineering, biomedical signal processing, electronic healthcare, millimeter wave radar, radar remote sensing, signal denoising.

I. INTRODUCTION

Most of the technical literature on contactless *vital signs monitoring* (VSM) focuses on the problems of estimating the average values of vital parameters (namely, *breath rate*, BR, and *heart rate*, HR), over a predetermined observation window, and detecting abnormal conditions including *apnea*, *bradycardia* or *tachycardia*; only a few publications address the problem of identifying the *exact* moment at which heartbeats occur. The detection of these events makes it possible to assess *heart rate variability* (HRV) by measuring *interbeat intervals* (IBIs). The interest in HRV is motivated by the fact that it conveys important information, being correlated with psychophysical health conditions of patients [1], and allows to predict the onset of heart diseases [2], [3].

Contactless VSM can be performed through different sensors such as lasers, lidars, cameras or radars. The measurements provided by the first three types of devices are severely affected by light conditions and accessories worn by the subject being monitored (such as clothes, glasses, etc.); on the contrary, those acquired through radars have been shown to provide the required accuracy, without being influenced by environmental factors or clothing. Moreover, radars inherently guarantee the privacy of the monitored subject [4], [5].

In the technical literature on radar-based methods for VSM, few manuscripts specifically address the problem of HRV estimation. The available solutions to this problem exploit *deep learning* (DL) algorithms or deterministic estimation techniques. On the one hand, the use of DL has been proposed in [6], [7], and [8]. In particular, a *recurrent neural network* (RNN) has been exploited in [6] to estimate the IBI and the sequences forming the cardiac cycle on the basis of the measurements of a 24 GHz *continuous wave* (CW) radar. In [7], template matching based on a *convolutional neural network* (CNN) has been used for extracting HR from the measurements obtained through a 77 GHz *multiple-input multiple-output* (MIMO) *frequency modulated continuous*

The associate editor coordinating the review of this manuscript and approving it for publication was Cheng Hu.

© 2024 The Authors. This work is licensed under a Creative Commons Attribution 4.0 License.
For more information, see https://creativecommons.org/licenses/by/4.0/

wave (FMCW) radar. Specifically, a network composed of multiple *one-dimensional* (1D) CNN layers has been developed to transform the displacement signal originating from the human chest into a *seismocardiogram* (SCG) signal for the estimation of the position of fiducial points. The use of a hybrid DL model combining a CNN and a *long short-term memory* (LSTM) network has been proposed in [8] to detect the P-wave, T-wave, and R peaks from measurements of a 24 GHz Doppler sensor.

On the other hand, various deterministic algorithms for HRV estimation have been proposed in [9] and [10]. It is important to mention that the algorithms illustrated in [9], [11] and [12] rely not only on radar measurements, but also on additional information coming from other sensors. In particular, in [9] multiresolution analysis (originally proposed in [13]) and template matching are employed to estimate IBIs through a 2.4 GHz CW Doppler *single-input single-output* (SISO) radar. However, the template is derived from a segment of a filtered photoplethysmograph signal. The approach to HRV assessment proposed in [11] is based on adaptive filtering. In fact, in this case, Wiener filtering is exploited to process the measurements provided by a 5.8 GHz SISO CW Doppler radar in order to highlight individual beats and facilitate their subsequent detection. However, filter weights result from a *least-square error* approach that aims at minimizing the mean squared distance between the filtered radar signal and a reference *electrocardiogram* (ECG) signal. This solution is affected by the intrinsic non-stationarity of the radar signal, making the filter weights usable over a limited time interval. A *three-dimensional* (3D) lidar for pose detection is used in [12] in order to acquire position information about the subject to be monitored. This information is exploited to accomplish precise beam-forming in a MIMO Doppler radar. Moreover, the Viterbi algorithm is used to identify heart-related peaks in radar measurements.

The remaining deterministic methods do not require additional sensors and utilize filtering techniques based on cardiac physiology for HRV estimation. Furthermore, all these methods employ SISO CW Doppler radars operating at 24 GHz. Specifically, the method proposed in [14] assumes that IBIs vary slowly over time and applies the Viterbi algorithm. The metric for the Viterbi algorithm is designed to minimize the difference between the IBIs throughout the acquisition period and the average IBI over the same duration. The use of the Viterbi algorithm has been also proposed in [15] and [16]. More specifically, on the one hand, a modified Viterbi algorithm is employed in [15] to build a binary mask limiting the search for cardiac peaks over the radar signal. On the other hand, a Viterbi algorithm with mixed branch metrics, composed of a factor inspired by cardiac physiology and a factor learned through DL, is described in [16]. Finally, a conceptually different approach has been adopted in [10]. In fact, in this case, the proposed technique first detects all the peaks appearing in the radar signal and, then, classifies them as cardiac or spurious. Unfortunately, if the analyzed signal does not exhibit a peak at an instant at which there should be one, this technique is unable to recover it.

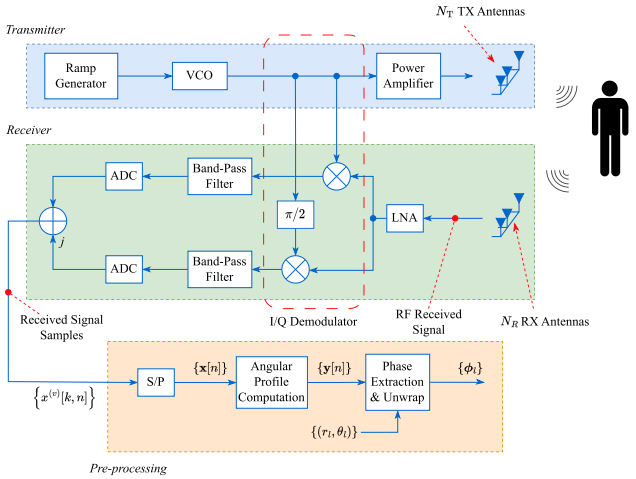

FIGURE 1. Block diagram of the colocated MIMO FMCW radar system considered in this manuscript.

In this manuscript, a novel deterministic method, called *PHYsiology-inspired Heart Rate Variability Estimator* (PHYHRVE) and able to detect each cardiac event (i.e., individual heartbeats) of a single healthy subject through the measurements provided by a colocated MIMO radar of FMCW type, is proposed. Its main features can be summarized as follows:

1) It processes the measurements acquired through a radar illuminating the whole body of the monitored subject. This makes available a set of measurements originating from different points of his/her body.

2) It exploits a selection combining strategy, since it discards the measurements that do not provide significant cardiac information. This significantly mitigates the impact of measurement noise and *random body movements* (RBMs).

3) Its development is partly inspired by the knowledge of the physiological mechanisms characterizing a healthy cardiovascular system. Such knowledge allows us to adopt a heuristic approach to the problems of a) filtering the available radar measurements and b) searching for cardiac peaks in the filtered signal. For this reason, our method can be considered as a form of *physiology inspired processing*.

The remaining part of this manuscript is organized as follows. In Section II, a brief description of a colocated MIMO radar system is provided; moreover, we show how VSM information can be extracted from radar signals. The PHYHRVE is developed in Section III, whereas its accuracy is analyzed in Section IV, where various experimental results are illustrated and commented. Finally, some conclusions are offered in Section V.

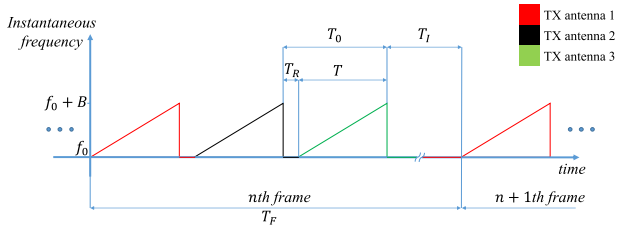

FIGURE 2. Representation of the temporal evolution of the instantaneous frequency characterizing the signal radiated by the MIMO radar system shown in Fig. 1 and operating in TDM mode; $N_T = 3$ is assumed.

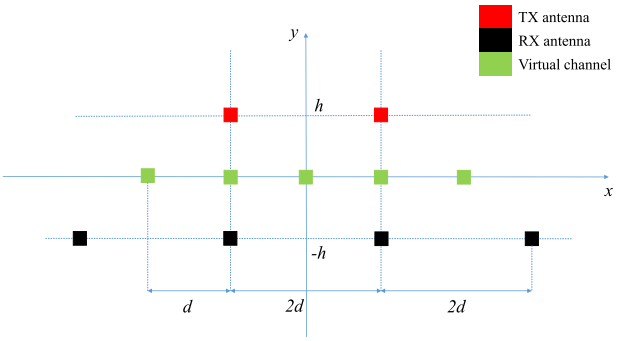

FIGURE 3. Representation of a ULA composed by 5 virtual elements; here, $N_R = 4$ and $N_T = 2$.

II. SYSTEM AND SIGNAL MODELS

In the following, we take into consideration a colocated MIMO FMCW radar equipped with N_T *transmit* (TX) and N_R *receive* (RX) antennas (these form the TX and RX arrays, respectively); its architecture is illustrated in Fig. 1. In this radar system, a *voltage controlled oscillator* (VCO), characterized by the free-running oscillation frequency f_0, is used to generate the signal radiated by each TX antenna. This signal consists of a sequence of *chirps*; the duration of the time slot assigned to each chirp is

$$T_0 = T + T_R, \tag{1}$$

where T and T_R represent the duration of the chirp (*ramp time*) and that of the interval separating two consecutive chirps (*reset time*), respectively. The transmission of chirps is organized according to *frames*; each frame is composed of N_T consecutive chirps, each transmitted by a different TX antenna since the radar system is assumed to operate in *time division multiplexing* (TDM) mode. For this reason, the duration of a single frame is

$$T_F = N_T T_0 + T_I, \tag{2}$$

where T_I, called *idle time*, is the duration of the time interval separating consecutive frames. The temporal evolution of the instantaneous frequency of the radiated signal is shown in Fig. 2, where $N_T = 3$ is assumed.

The electromagnetic signal radiated by the TX antennas is reflected by any target located within the radar *field-of-view* (FOV). If the radar is used for VSM, the most significant portion of the reflected signal (i.e., of the radar *echo*), originates from the body of the monitored subject and is influenced by the temporal evolution of the displacement of the body itself. In the case of VSM, the displacement consists of [17]: a) relatively large movements caused by *inspiration and expiration phases*; b) small oscillations caused by cardiac activity; c) RBMs having unpredictable amplitude. These elements can contribute differently to the displacement based on: a) the orientation and the distance of the body with respect to the radar; b) the psychophysical state of the monitored subject. For instance, if the subject is resting, relaxed, and in a comfortable position, it is reasonable to assume that the contribution of his/her RBMs to the overall displacement is almost negligible.

As shown in Fig. 1, the electromagnetic echo is captured by the RX array. Each of the N_R received signals undergoes amplification, quadrature downconversion, and analog-to-digital conversion; these tasks are performed by a *low noise amplifier* (LNA), a couple of mixers & bandpass filters, and a couple of *analog-to-digital converters* (ADCs), respectively. It is important to mention that, in the considered radar systems, a set of independent measurements is generated for each pair of physical TX and RX antennas. This is due to the fact that each of the $N_V \triangleq N_T N_R$ TX/RX antenna pairs can be replaced by a single *virtual antenna* (VA) of an equivalent SISO radar [18]. The abscissa x_v and ordinate y_v of the vth VA associated with the pth TX antenna and the qth RX antenna are computed as

$$x_v = \frac{x_p + x_q}{2} \tag{3}$$

and

$$y_v = \frac{y_p + y_q}{2}, \tag{4}$$

respectively, with $p = 0, 1, \ldots, N_T - 1$, $q = 0, 1, \ldots, N_R - 1$, and $v = 0, 1, \ldots, N_V - 1$; here, (x_p, y_p) and (x_q, y_q) denote the coordinates[1] of the pth TX and qth RX antennas, respectively. These concepts are exemplified by Fig. 3, where a specific case of TX and RX physical arrays, and the resulting virtual array are shown. Note that, in this case, the virtual array is a *uniform linear array* (ULA), as it consists of $N_V = 6$ equally spaced and aligned virtual elements, and that two distinct virtual elements overlap.

If in the radar FOV there is a single point target whose distance from the radar oscillates around the value R_0, the kth complex sample acquired through the vth VA in the nth frame can be approximated as (see, e.g., [19, Sec. 2.1.2, eq. (5)])

$$x^{(v)}[k, n] \simeq a^{(v)} \exp\left(j(2\pi k f_n T_s + \psi^{(v)}[n])\right) + w^{(v)}[k, n], \tag{5}$$

with $v = 0, 1, \ldots, N_V - 1$ and $k = 0, 1, \ldots, N - 1$; here, T_s is the sampling period, N is the total number of

[1] We assume that the TX and RX arrays lie on the same plane.

samples acquired during a single chirp interval, $w^{(v)}[k,n]$ is the complex Gaussian noise sample affecting $x^{(v)}[k,n]$, and $a^{(v)}$, f_{n}, and $\psi^{(v)}[n]$ denote the amplitude, frequency, and phase, respectively, of the useful component of $x^{(v)}[k,n]$. It can be shown that (e.g., see [20, Sec. II-C])

$$f_{\mathrm{n}} = \frac{2\mu R_0}{c} \tag{6}$$

and

$$\psi^{(v)}[n] = \frac{4\pi}{\lambda} R^{(v)}[n], \tag{7}$$

where $\mu = B/T$ is the chirp slope, B is the swept frequency interval (i.e., the radar bandwidth), $\lambda = f_{\mathrm{c}}/c$ is the radar wavelength, and $R^{(v)}[n]$ is the distance of the vth VA from the considered point target during the nth frame interval. Based on the assumptions made on the target range (i.e., on the distance between the target and the radar), (7) can be rewritten as

$$\psi^{(v)}[n] = \psi_0 + \Delta\psi^{(v)}[n], \tag{8}$$

where

$$\psi_0 = 4\pi \frac{R_0}{\lambda} \tag{9}$$

is a constant phase shift depending on the distance R_0 and

$$\Delta\psi^{(v)}[n] = \frac{4\pi}{\lambda} \Delta R^{(v)}[n] \tag{10}$$

represents the phase shift caused by the range variation $\Delta R^{(v)}[n] \triangleq R^{(v)}[n] - R_0$.

The sample stream $\{x^{(v)}[k,n]\}$, conveying the measurements acquired from all the VAs, feeds a *pre-processing* stage, where it is partitioned into blocks; each block collects the measurements acquired over N_{F} consecutive frames. Moreover, the measurements of a single block are arranged in a 3D array, called *radar cube* and represented on the left side of Fig. 4. Note that, in that figure, the slow time index corresponds to the frame index, whereas the fast time index corresponds to the index of signal samples originating from a single chirp; for this reason, the size of the radar cube is $(N_{\mathrm{F}} \times N_{\mathrm{V}} \times N)$. In the remaining part of this section, we describe the pre-processing executed on the radar cube collecting the frames associated with $n = 0, 1, \ldots, N_{\mathrm{F}} - 1$. In our description, it is assumed that:

a) The available VAs form a horizontal ULA; this makes it possible to estimate both the range and azimuth of detectable targets.

b) The electromagnetic signals radiated by the considered MIMO radar illuminate the whole body of the monitored subject (see Section IV).

c) The position of the body with respect to the radar system is known with reasonable accuracy.[2]

The pre-processing evolves through the steps described below.

1. *Computation of angular profile* - In this step, the so-called *angular profile* (AP) is evaluated on a frame-by-frame basis (this corresponds, in our representation of the radar cube, to taking the measurements forming different vertical slices, each associated with a different value of n). The matrix collecting the measurements $\{x^{(v)}[k,n]\}$ associated with a given n undergoes zero padding followed by an order (N_0, N_1) *two-dimensional* (2D) *discrete Fourier transform* (DFT),[3] where $N_0 \triangleq N \cdot M_0$, $N_1 \triangleq N_{\mathrm{V}} \cdot M_1$, and M_0 and M_1 represent the oversampling factors adopted along the fast time and the slow time, respectively; the element (p, q) of the DFT output is

$$y^{(n)}[p,q] = \frac{1}{N_0 N_1} \sum_{v=0}^{N_{\mathrm{V}}-1} \times \sum_{k=0}^{N-1} x^{(v)}[k,n] \exp\left(-j2\pi\left(\frac{k}{N_0}p + \frac{v}{N_1}q\right)\right), \tag{11}$$

with $p = 0, 1, \ldots, N_0 - 1$ and $q = 0, 1, \ldots, N_1 - 1$. The evaluation of the 2D DFT generates the AP associated with the nth frame; such a profile is a $N_0 \times N_1$ matrix of complex samples and provides a spatial description of the radar echo in range/azimuth coordinates. For this reason, it allows us to detect the presence of targets, and to estimate their range and azimuth. In our use case, the strong echoes detected by the radar are generated by various parts of the human body illuminated by the radar itself: being the body an extended target, it shows itself in the AP as a multitude of reflections characterized by various range-azimuth combinations. An example of the amplitude information conveyed by a specific angular profile is offered in the lower part of Fig. 4. Note also that, because of the use of an order (N_0, N_1) 2D DFT, the computation of the AP leads to partitioning the range-azimuth space in front of the radar system into $N_0 \cdot N_1$ spatial cells or *bins*.

Repeating the 2D DFT processing described above for $n = 0, 1, \ldots, N_F - 1$ generates N_F distinct APs, whose elements can be organized in the new radar cube appearing on the right side of Fig. 4 and called *AP radar cube*.

2. *Phase extraction and unwrapping* - In this step, phase information is extracted from the AP radar cube. This step is accomplished as follows. First, we identify, for a given n, all the AP bins corresponding to different points of the body of the monitored subject.[4] Note that bin selection can be accomplished at the beginning of the monitoring procedure by exploiting our prior knowledge about the position of the body with respect to the radar system (further details are provided in Section IV). Then, the selected bins can be kept for successive acquisitions, if the patient-radar relative position undergoes negligible changes. The spatial

[2]The AP region in which the echoes from the body are visible should be delimited in such a way that other strong reflections do not fall in that region.

[3]The 2D DFT can be efficiently computed using a 2D *fast Fourier transform*.

[4]These points correspond to distinct parts of the body such as the head, chest, abdomen, belly, etc. (see Fig. 13).

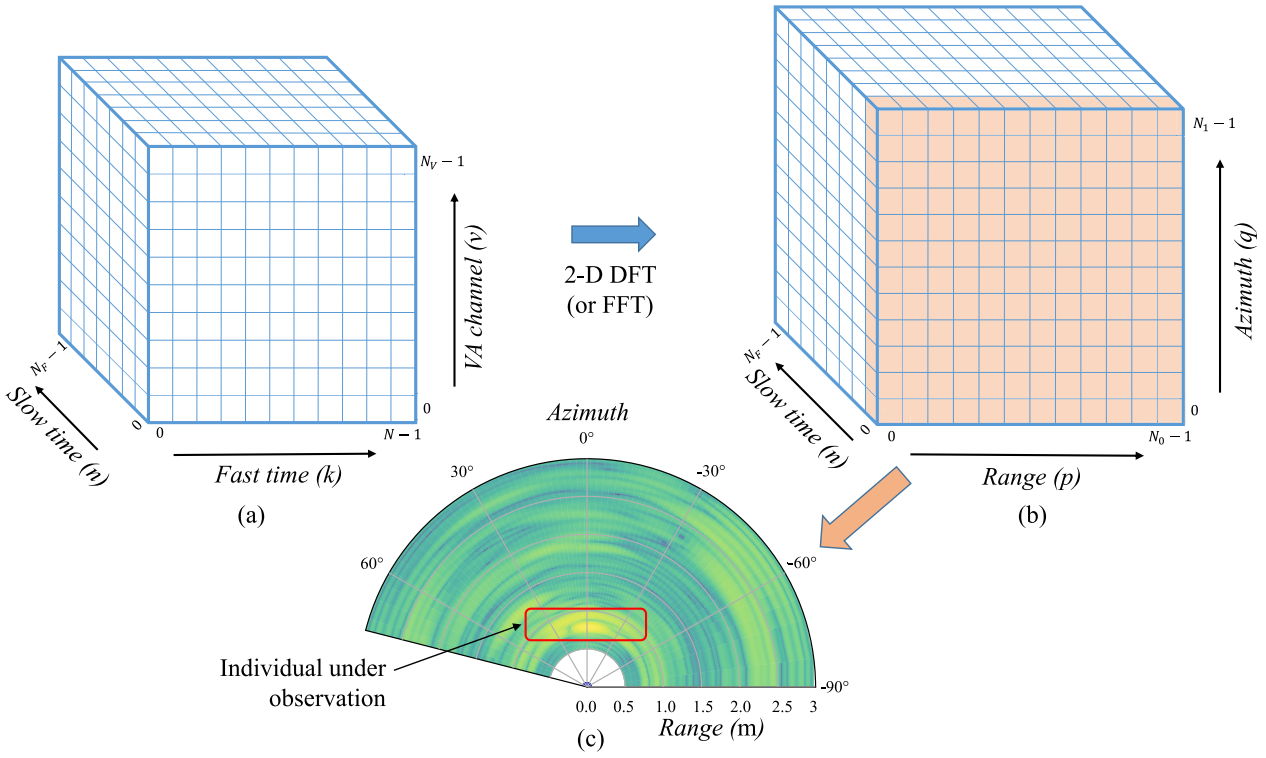

FIGURE 4. Representation of: a) a radar cube; b) its associated AP radar cube, and; c) the amplitude information conveyed by a single AP (i.e. that highlighted in orange in the AP radar cube) in the presence of a single supine individual at approximately 1 m distance from the radar system.

coordinates of the selected bins are collected in the L-dimensional set $\{(p_l, q_l); l = 1, 2, \ldots, L\}$, where $p_l \in \{0, 1, \ldots, N_0 - 1\}$ and $q_l \in \{0, 1, \ldots, N_1 - 1\}$ denote the range index and the angle index, respectively, of the lth bin, and L represents the overall number of considered bins. The elements of the set $\{(p_l, q_l)\}$ are used to extract the phase of the corresponding AP points through the so-called *arctangent demodulator* [21]. Therefore, the phase associated with the lth AP bin and the nth frame is evaluated as

$$\phi_l[n] = \arctan\left(\frac{y_l^{(Q)}[n]}{y_l^{(I)}[n]}\right), \tag{12}$$

where $y_l^{(Q)}[n] \triangleq \Im\{y^{(n)}[p_l, q_l]\}$ and $y_l^{(I)}[n] \triangleq \Re\{y^{(n)}[p_l, q_l]\}$. Then, $\phi_l[n]$ undergoes *unwrapping*; this produces the *unwrapped phase*

$$\tilde{\phi}_l[n] = \begin{cases} \phi_l[n], & \text{if } |\phi_l[n] - \phi_l[n-1]| \leq \pi \\ \phi_l[n] - 2\pi, & \text{if } \phi_l[n] - \phi_l[n-1] > \pi \\ \phi_l[n] + 2\pi, & \text{if } \phi_l[n] - \phi_l[n-1] < -\pi, \end{cases} \tag{13}$$

for $n = 0, 1, \ldots, N_F - 1$ and $l = 1, 2, \ldots, L$. This concludes our description of the pre-processing stage. Such a stage deserves the following comments:

Physiological aspects and considerations about the adopted measurement setup - It is important to stress that radar-based systems for VSM detect the mechanical movement of the patient's chest, i.e. measure its displacement. This displacement is generated by the sequential occurrence of multiple events originating from the anatomical and functional structures of the cardiovascular system, such as the *mitral valve closure*, the *isovolumic contraction*, the *aortic valve opening*, the *rapid ejection*, the *aortic valve closure*, the *mitral valve opening*, and the *rapid filling* [22]. *Seismocardiography*, a discipline that exploits chest movements for the diagnosis and early detection of heart diseases or cardiovascular malfunctions, precisely describes the components of the displacement signal and the physiological mechanisms that generate them [23]. For this reason, a SCG, i.e. the recording of body vibrations induced by the heart beat has a richer information content than an ECG, that, by definition, is generated on the basis of measured electrical signals. The displacement detected by a radar system, being a contactless variant of a SCG, also contains multiple pieces of information (additional details about this are provided in Section III).

On the benefits of spatial diversity - As aforementioned, phase information is extracted from multiple spatial bins, providing a significant source of *spatial diversity*, which stems from: 1) the fact that the monitored subject, as an extended target, generates a large number of echoes; and 2) the ability, enabled by the use of antenna arrays, to capture echoes from different directions. The idea of exploiting this form of diversity is not new in the VSM literatures [24], [25], [26], and [27]. More specifically, the use of a couple of *impulse radio - ultra wideband* (IR-UWB) radars is proposed

in [24] and [25] to improve the accuracy and robustness of HR and BR estimation, even in the presence of large body movements. In [26], the signals provided by multiple VAs of a MIMO FMCW radar are combined to improve the detection of BR and HR. In [27], it is shown that, in the case of FMCW radars, the coherent combination of signals from adjacent range bins containing cardiac and respiratory information allows to improve the overall *signal-to-noise ratio* (SNR) in HR estimation. However, as far as we know, no previous work has exploited the information originating from multiple spatial points, characterized by different range-angle coordinates, for HR estimation. As illustrated in Section IV, our experimental results have evidenced that, if a MIMO FMCW radar is available, useful cardiac information can be acquired from multiple bins of the AP, which *do not necessarily* correspond to adjacent points of the body of the monitored subject. This is due to the fact that the vibrations generated by the cardiovascular system propagate throughout the body via the circulatory system and tissues. In agreement with [28], our experimental results have led us to the conclusion that, as a matter of fact, any point of the body is influenced by cardiac vibrations. Therefore, in principle, any bin of the AP associated with a point of the monitored body conveys potentially useful information for HR estimation [29]. However, as evidenced by our experimental results, the displacement signals associated with different AP bins may exhibit substantially different shape, amplitude and spectral content [29]. This is exemplified by Figs. 5-a), 5-b) and 5-c), that show the time evolution of the unwrapped phases originating from three different AP bins; two of them are associated with two distinct points of the monitored body, whereas the remaining one is associated with a stationary object.[5] The first signal is characterized by a well defined periodicity due to the thoracic movement caused by breathing; the small perturbations superimposed with its periodic trend are due to cardiac activity. The second signal, instead, exhibits a completely different trend, which is affected by large variations due to a lower SNR. The variability observed in the quality of displacement signals captured from the same body (i.e., the first and second signals) is mainly due to the following causes:

a) Points located across the entire surface of the body are characterized by a different angle of incidence of the electromagnetic waves radiated by the radar. Consequently, the *shape* of the signal associated with a single respiratory period changes from point to point;

b) Spatially disjoint points reflect electromagnetic radiation differently; this results in signals having different signal strengths and, consequently, different SNRs;

[5]Since bin selection is accomplished manually at the beginning of acquisitions, one or more spatial coordinates included in the set $\{(p_l, q_l); l = 1, 2, \ldots, L\}$ may not correspond to AP bins associated with parts of the monitored body, but to closely located stationary objects (e.g., the bed on which the body is lying).

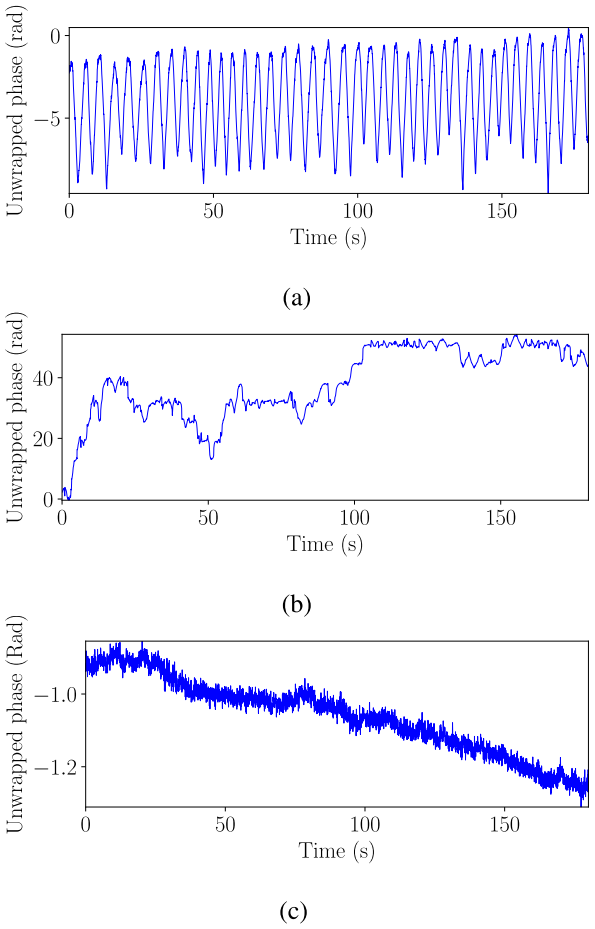

FIGURE 5. Unwrapped phase signals acquired from three distinct AP bins: a) phase signal exhibiting a periodic trend due to respiration and small perturbations caused by cardiac activity; b) phase signal acquired in the same observation interval, but corrupted by RBMs; c) phase signal acquired in the same observation interval, but originating from a stationary object.

c) RBMs and slight movements are more frequent in certain parts of the body (such as its extremities), but they may be entirely absent in others.

As far as the third signal is concerned, instead, the following considerations can be made:

a) even if the object from which it originates is still, small fluctuations are visible in its time evolution. These are mainly due to the phase noise affecting the radar and to the propagation of cardiac vibrations to that object;

b) its amplitude variations are significantly lower than those observed for the other two signals.

III. ESTIMATION OF INTERBEAT INTERVALS

The inner structure of the PHYHRVE is described by the block diagram shown in Fig. 6. The tasks performed by each of its blocks are described below.

1. *First filtering stage* - For any l, the unwrapped phase sequence $\{\tilde{\phi}_l[n]\}$ can be represented as the superposition of multiple overlapped components (including noise); the most dominant of them is due to the respiratory activity

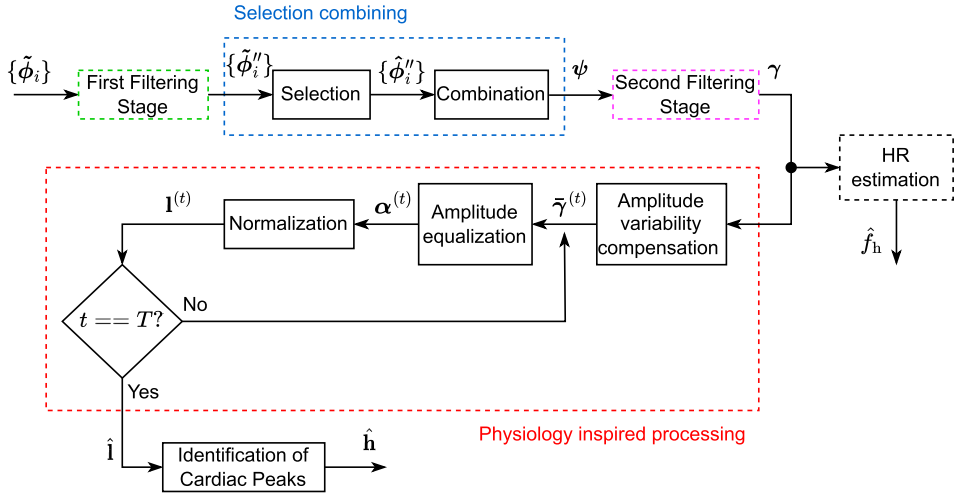

FIGURE 6. Block diagram of the PHYHRVE.

of the monitored subject, since its displacement is typically ten times wider than that of the component produced by the cardiac activity [11]. Since we are interested in HR estimation only, the respiratory component represents a form of disturbance and needs to be cancelled. The method we adopt to achieve this target is based on the evaluation of the new sequence $\{\tilde{\phi}_l''[n]\}$, whose nth element is defined as

$$\tilde{\phi}_l''[n] \triangleq \tilde{\phi}_l[n+2] - 2\tilde{\phi}_l[n+1] + \tilde{\phi}_l[n], \tag{14}$$

for $n = 0, 1, \ldots, N_F - 3$. This sequence, called lth *enhanced heartbeat signal* (EHS), can be interpreted as the *second derivative* of $\{\tilde{\phi}_l[n]\}$. In fact, (14) can be rewritten as

$$\tilde{\phi}_l''[n] \triangleq \tilde{\phi}_l'[n+1] - \tilde{\phi}_l'[n], \tag{15}$$

where

$$\tilde{\phi}_l'[n] \triangleq \tilde{\phi}_l[n+1] - \tilde{\phi}_l[n] \tag{16}$$

represents the *first derivative* of $\{\tilde{\phi}_l[n]\}$. The impact of the first and second derivatives on the unwrapped phase sequences is exemplified by Fig. 7, in which the spectra of the phase signal represented in Fig. 5-a), of its first derivative and its second derivative are shown. Note that: a) the evaluation of the second derivative reduces the amplitude of the spectral peak originating from respiration, but enhances that of the spectral peak associated with cardiac activity; b) using the first derivative only requires additional band-pass filtering to remove the residual contribution of respiration, whose strength is still significant.

2. *Signal selection and generation of a single sequence for HRV estimation* - The considerations previously illustrated for the displacement signals shown in Figs. 5-a), 5-b) and 5-c) (see Section II) also apply to the associated EHSs, that are shown in Figs. 8-a), 8-b) and 8-c), respectively (in all those figures the instants at which cardiac peaks occur are identified by red vertical lines). In fact, on the one hand, the peaks characterizing the EHS shown in Fig. 8-a) occur at the

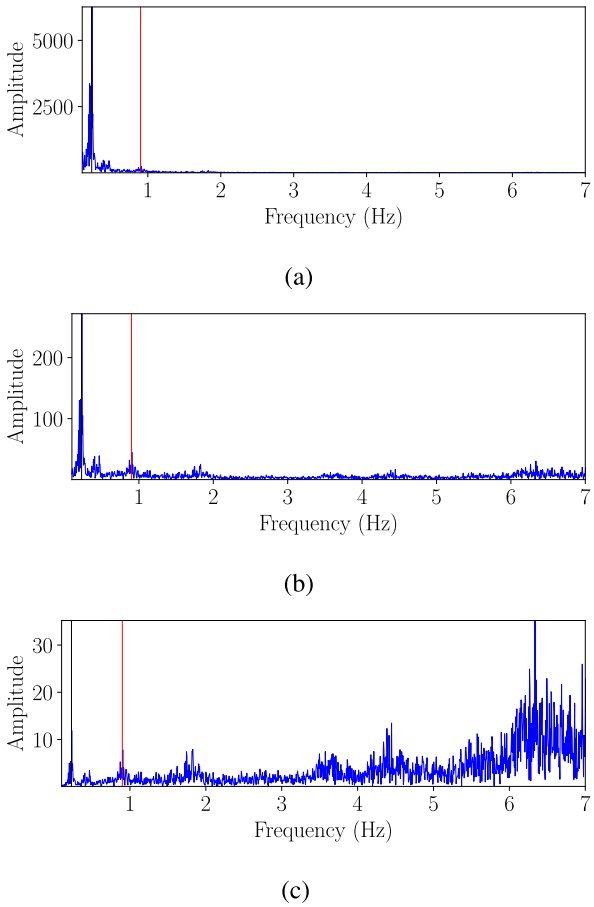

FIGURE 7. Representation of the spectrum of: a) the unwrapped phase signal shown in Fig. 5-a; b) its first derivative; c) its second derivative. The respiratory peak is identified by a black vertical line (indicating the exact BR), whereas the cardiac peak by a red vertical line (indicating the exact HR).

right instants and have comparable amplitudes. On the other hand, the signals shown in Fig. 8-b) and Fig. 8-c) do not

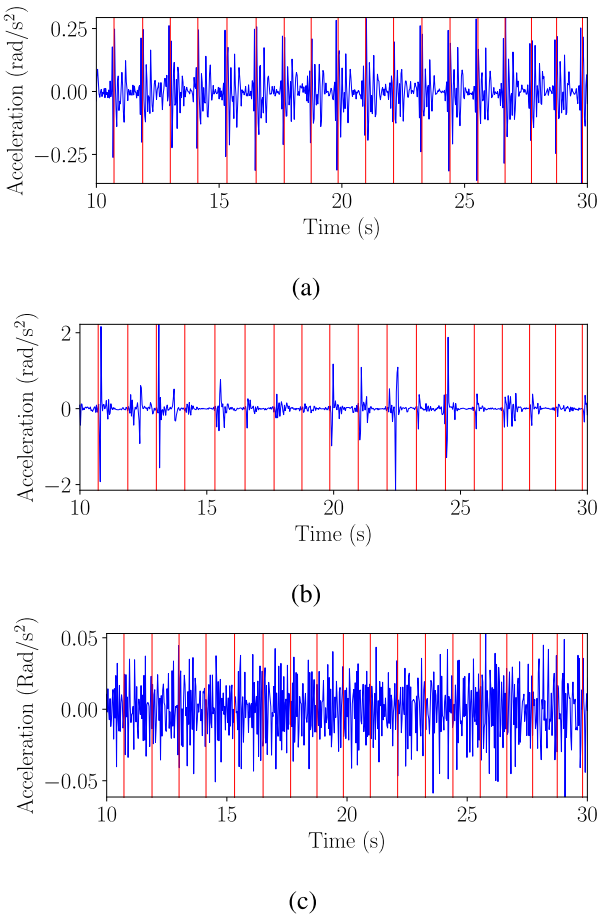

FIGURE 8. Representation of: a) an EHS containing relevant cardiac information; b) an EHS corrupted by RBMs, and; c) an EHS obtained from the observation of a stationary object. The instants at which cardiac beats occur are provided by an additional sensor and identified by vertical red lines.

share these properties. The first EHS, in particular, contains various spikes caused by RBMs (such spikes are visible at $t = 12$, 16, 25, and 29 s). This motivates the adoption of a strategy for selecting the best EHSs (i.e., a *selection combining* strategy); once the best signals have been selected, they can be combined to generate a single signal on the basis of which the occurrence of cardiac peaks is detected.

These ideas are put into practice by first selecting the most relevant EHSs and, then, by combining them. The selection of the most relevant EHSs is accomplished as follows. First, the covariance between the lth and the jth EHSs is evaluated as

$$W_{l,j} \triangleq \frac{\sum_{n=0}^{N_F-3} \left(\tilde{\phi}_l''[n] - \eta_{\tilde{\phi}''}[l]\right) \cdot \left(\tilde{\phi}_j''[n] - \eta_{\tilde{\phi}''}[j]\right)}{N_F - 2} \quad (17)$$

for any j and l, with $j \neq l$; here,

$$\eta_{\tilde{\phi}''}[l] \triangleq \frac{1}{N_F - 2} \sum_{n=0}^{N_F-3} \tilde{\phi}_l''[n]. \quad (18)$$

represents the *time average* of the lth EHS (with $l = 1, 2, \ldots, L$). Then, the *quality index*

$$Q_l \triangleq \sum_{j \in \mathcal{S}_l} \bar{W}_{l,j}, \quad (19)$$

is computed for lth EHS, with $l = 1, 2, \ldots, L$; here, $\mathcal{S}_l \triangleq \{1, 2, \ldots, l-1, l+1, \ldots, L\}$ and

$$\bar{W}_{l,j} \triangleq \begin{cases} W_{l,j} & \text{if } W_{l,j} \geq 0 \\ 0 & \text{if } W_{l,j} < 0. \end{cases} \quad (20)$$

Finally, the $\hat{L}$ EHSs characterized by the largest values of the quality index (19) are chosen; the ith sequence resulting from this selection is denoted $\{\hat{\phi}_i''[n]\}$, with $i = 0, 1, \ldots, \hat{L} - 1$. These EHSs are combined to generate a single EHS, denoted $\{\psi\}$. This result is achieved by summing the sequences $\{\{\hat{\phi}_i''[n]\}; i = 0, 1, \ldots, \hat{L} - 1\}$ in an element-wise fashion and removing their time averages. Therefore, we have that

$$\psi[n] = \sum_{i=0}^{\hat{L}-1} \hat{\phi}_i''[n] - \eta_{\hat{\phi}''}[i], \quad (21)$$

for $n = 0, 1, \ldots, N_F - 3$; here,

$$\eta_{\hat{\phi}''}[l] \triangleq \frac{1}{N_F - 2} \sum_{n=0}^{N_F-3} \hat{\phi}_l''[n]. \quad (22)$$

represents the time average of $\{\hat{\phi}_l''[n]\}$ (see (18)).

3. *Second filtering stage* - This block aims at detecting the envelope of the sequence $\{\psi[n]\}$. First of all, the absolute value of each sample available at the output of the previous block is taken. This generates the new sequence $\{\xi[n]\}$, whose nth element is defined as

$$\xi[n] \triangleq |\psi[n]| \quad (23)$$

for $n = 0, 1, \ldots, N_F - 3$. Then, the sequence $\{\xi[n]\}$ is applied to a moving average filter, characterized by a window size equal to M. The value of M should be selected in such a way that the time interval MT_F approximately corresponds to half the minimum expected distance between two consecutive heartbeats of a healthy subject. The filter output is the new sequence

$$\{\gamma[n]; n = 0, 1, \ldots, N_F - M - 3\}. \quad (24)$$

The typical trend of the sequence $\{\psi[n]\}$ and that of the associated sequence $\{\gamma[n]\}$ are illustrated in Fig. 9, where the ECG curve acquired for the same subject in a given observation interval (lasting 20 s) is also shown. It is important to note that:

a) The evaluation of the absolute value in (23) is justified by our experimental results, which show that the R peaks can appear as either positive or negative peaks in the sequence $\{\psi[n]\}$. This variability is primarily due to the differences in the points detected on the monitored subject's body, as well as to the variations in their physiology and conditions.

b) As already mentioned in Section II, being the time evolution of $\{\psi[n]\}$ similar to that of an SCG signal, its

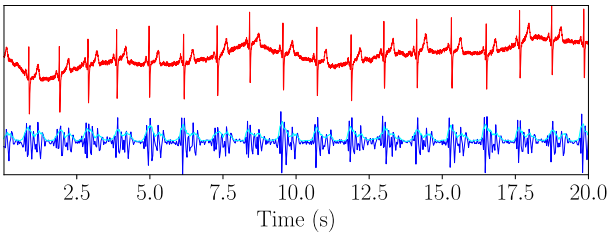

FIGURE 9. Representation of: a) the sequence $\{\psi[n]\}$ acquired from a specific subject over an observation interval lasting 20 s (blue curve); b) the associated sequence $\{\gamma[n]\}$ (cyan curve); c) the ECG acquired from the monitored subject in the same observation interval (red curve).

information content is richer than that of the corresponding ECG.

c) A single local maximum is observed in the sequence $\{\gamma[n]\}$ in correspondence with each ECG R peak. However, each maximum originates from the presence of multiple peaks appearing in the sequence $\{\psi[n]\}$ and surrounding it. Evaluating the timing of each cardiac event on the basis of the position of each local maximum of $\{\gamma[n]\}$ would not be easy and, consequently, would not lead to a precise estimation of the IBIs.

d) The shapes of the bursts of peaks appearing in the sequence $\{\gamma[n]\}$ in correspondence with cardiac events are all different, i.e. do not follow a repetitive pattern. Moreover, their amplitude is time varying. As a result, the detection of cardiac events on the basis of the sequence $\{\gamma[n]\}$ becomes more difficult: setting a fixed threshold on its amplitude does not represent a viable solution.

The above mentioned phenomenon of *amplitude variability* plays an important role in the development of the following processing stages. Its presence can be explained as follows. The propagation of cardiac vibrations within the body and through the cardiovascular system is influenced by the psychophysical state of the monitored subject. For instance, the amplitude of cardiac peaks appearing in the sequence $\{\gamma[n]\}$ is influenced by the respiratory phase. In fact, our measurements have evidenced that, during the inspiration pause,[6] the amplitude of these peaks is significantly lower than that characterizing other respiratory phases. This phenomenon, described also by Will et al. [30], can be observed in Fig. 10-a), where the sequence $\{\gamma[n]\}$ is represented over a time interval lasting 50 s. For instance, in the intervals (24, 26) s and (34, 39) s, in which the employed reference sensor (red curve) detects the occurrence of inspiration pauses, a lower amplitude is observed in the peaks of the sequence $\{\gamma[n]\}$.

In the remaining part of the PHYHRVE, the sequence $\{\gamma[n]\}$ (24) undergoes further processing in order to:

a) Extract the average HR;

b) Attenuate the intrinsic amplitude variability caused by respiration, as explained above;

[6]The inspiration pause is the respiration phase immediately following the inspiration phase. During the inspiration pause, the lungs are full of air.

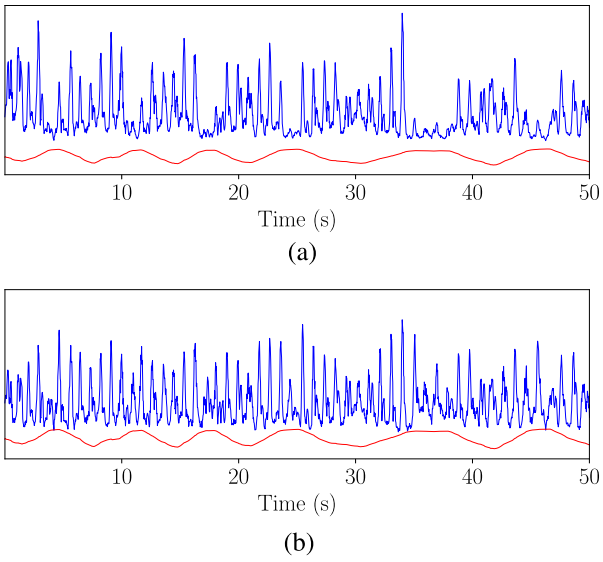

FIGURE 10. Representation of: a) a sequence $\{\gamma[n]\}$ characterized by a significant amplitude variability (blue curve) and the associated breath reference; b) the corresponding sequence $\{\bar{\gamma}[n]\}$.

c) Enhance the peaks of the sequence $\{\gamma[n]\}$ that really correspond to R peaks and attenuate the remaining ones.

This result is achieved by multiplying each element of the sequence $\{\gamma[n]\}$ by a time-varying gain that: a) strengthens the peaks appearing periodically or quasi-periodically, and spaced apart by a time interval close to the inverse of the average HR; b) attenuates the other ones. In the following, this part of the overall processing is called *amplitude equalization*; moreover, relevant peaks are dubbed *cardiac peaks*, whereas non-relevant ones *spurious peaks*.

d) Apply a form of *normalization* to the sequence resulting from the amplitude equalization of $\{\gamma[n]\}$. This makes the heights of cardiac peaks comparable, so making the subsequent detection of such peaks easier.

4. *Estimation of average heart rate* - The estimation of the average HR is obtained by applying the so-called *periodogram method* [31] to the sequence $\{\gamma[n]\}$ (24). For this reason, this sequence undergoes zero padding (that produces the zero-padded sequence $\{\gamma_{zp}[k]\}$, followed by an order N_0' DFT; here, $N_0' = M_0' \cdot (N_F - M - 2)$, where M_0' denotes the selected oversampling factor. This produces the N_0-dimensional complex sequence $\{\Gamma[n]\}$, where

$$\Gamma[n] = \frac{1}{N_0'} \sum_{k=0}^{N_F-M-3} \gamma_{zp}[k] \exp(-j2\pi kn/N_0'), \tag{25}$$

for $n = 0, 1, \ldots, N_0' - 1$. Then, the HR estimate is computed as

$$\hat{f}_h = \frac{\hat{h}_h}{N_0 T_F} \tag{26}$$

where

$$\hat{h}_h = \arg \max_{h \in \{h_{min}, \ldots, h_{max}\}} |\Gamma[h]|, \tag{27}$$

and $h_{\min}$ and $h_{\max}$ represent the indices of the DFT bins associated with the maximum and minimum physiological HRs,[7] respectively.

5. *Amplitude variability compensation* - As already discussed in this section, the amplitude variability of the sequence $\{\gamma[n]\}$, mainly caused by respiration, must be compensated for. This task is carried out by dividing each element of the sequence $\{\gamma[n]\}$ by its low-pass filtered version. Filtering is accomplished by a 4th order Butterworth low-pass filter having cut-off frequency $f_{\text{cut}} = \hat{f}_{\text{h}}/2$. The output of this block is represented by the sequence

$$\{\bar{\gamma}[n]; n = 0, 1, \ldots, N_{\text{F}} - M - 3\}. \tag{28}$$

The sequence $\{\bar{\gamma}[n]\}$ resulting from the sequence $\{\gamma[n]\}$ represented in Fig. 10-a) is shown in Fig. 10-b). Note that the peaks appearing in the intervals (24, 26) s and (34, 39) s are enhanced by the employed procedure.

6. *Amplitude equalization and normalization of the resulting sequence* - The nth element of the sequence $\{\alpha[n]\}$, resulting from the *amplitude equalization* of the corresponding element of $\{\bar{\gamma}[n]\}$, is computed as

$$\alpha[n] = \bar{\gamma}[n] \cdot G[n] \tag{29}$$

for $n = 2i_{\max} + 1, \ldots, N_{\text{F}} - M - 3$. The time-varying gain $G[n]$ is defined as

$$G[n] \triangleq \sum_{q=i_{\min}}^{i_{\max}} \sum_{p=i_{\min}}^{i_{\max}} \bar{\gamma}[n-q]\bar{\gamma}[n-q-p]w(p-q) \tag{30}$$

for any n; here,

$$i_{\min} \triangleq \lfloor 0.3/T_{\text{F}} \rfloor, \tag{31}$$

$$i_{\max} \triangleq \lceil 1.2/T_{\text{F}} \rceil, \tag{32}$$

$$w(x) = \mathcal{N}(x; 0, \sigma^2) \tag{33}$$

and $\mathcal{N}(x; \mu, \sigma^2)$ is the probability density function of a Gaussian random variable having mean μ and variance σ^2. The computation of $G[n]$ on the basis of (30) can be motivated as follows. Let us assume that a peak is observed in the sequence $\{\bar{\gamma}[n]\}$ at the nth instant. Such a peak is likely to be relevant (i.e., a true cardiac peak) if other two peaks are observed p and $(p + q)$ instants earlier in the same sequence, with $p = q$ or $p \simeq q$; this is due to the fact that, in healthy subjects, the HR is expected to change slowly over three consecutive cycles of cardiac activity. When this occurs, the *right-hand side* (RHS) of (30) contains at least one significant term, so that the value $G[n]$ is not small and the peak is preserved in generating $\{\alpha[n]\}$ according to (29). Note, also, that:

a) The indices p and q cannot take on arbitrary values, since the distance between two consecutive beats always belongs to the interval (0.3, 1.2) s; this explains why both p and q belong to the set $\{i_{\min}, i_{\max}\}$, where $i_{\min}$ and $i_{\max}$ are defined by (31) and (32), respectively.

[7]The maximum and minimum physiological heart rates are commonly considered to be 200 bpm and 45 bpm, respectively [18].

b) The weight $w(p-q)$ has been inserted in the RHS of (30) to penalize the case in which $q \neq p$ with respect to that in which $q = p$. This is due to the fact that the event of two consecutive cycles having the same duration is deemed to be more likely than that associated with unequal temporal distances between consecutive cardiac peaks.

c) The adoption of the Gaussian function (33) in the evaluation of the weights is motivated by the fact that the difference between adjacent IBIs has been shown to be represented by a Gaussian distribution [32].

The sequence $\{\alpha[n]\}$ undergoes *normalization*; this generates the new sequence $\{l[n]\}$. The nth element of the normalized sequence is evaluated as

$$l[n] \triangleq \frac{\alpha[n] - \alpha_{\min}[n]}{\alpha_{\max}[n] - \alpha_{\min}[n]}, \tag{34}$$

for $n = 2i_{\max} + S + 1, \ldots, N_{\text{F}} - M - 3$; here

$$\alpha_{\min}[n] = \min_{\tilde{n} \in \{n, n+1, \ldots, n+2i_{\max}+S+1\}} \alpha[\tilde{n}] \tag{35}$$

and

$$\alpha_{\max}[n] = \max_{\tilde{n} \in \{n, n+1, \ldots, n+2i_{\max}+S+1\}} \alpha[\tilde{n}] \tag{36}$$

represent the minimum and maximum values, respectively, of $\{\alpha[n]\}$ observed over a specific time window, and S represents the so-called *normalization depth*. Note that, in practice, the normalization procedure requires S elements to start; therefore, these elements are lost, i.e., they do not have a normalized counterpart.

In our work, we have also explored the possibility of using the equalization-normalization procedure in an iterative fashion; this means that the sequence resulting from normalization undergoes a new amplitude equalization and, then, is normalized again. Our numerical results have led us to the conclusion that T equalization-normalization iterations further reduce spurious peaks while improving the visibility of cardiac peaks, provided that T is not large (say, $T \leq 3$). This idea is exemplified by Fig. 11, in which a specific sequence $\{\bar{\gamma}[n]\}$, and the corresponding sequences $\{l^{(1)}[n]\}$ and $\{l^{(2)}[n]\}$ generated by a single iteration and two iterations, respectively, of the proposed equalization-normalization procedure are illustrated. Note also that, if this strategy is employed, an iteration-dependent (and, in particular, a progressively decreasing) variance could be adopted in the evaluation of the weights according to (33) in order to improve the quality of the refinement process (the standard deviation adopted for the Gaussian function $w(x)$ (33) in the kth iteration is denoted $\sigma^{(k)}$). In the following, independently of the value of T, the final sequence resulting from a single or multiple equalization normalization steps is denoted $\{\hat{l}[n]\}$.

7. *Identification of cardiac peaks* - The last step consists of identifying the instants at which cardiac peaks appear in the sequence $\{\hat{l}[n]\}$. Further details about the specific solution adopted in our implementation of the PHYHRVE are provided in Subsection IV-B.

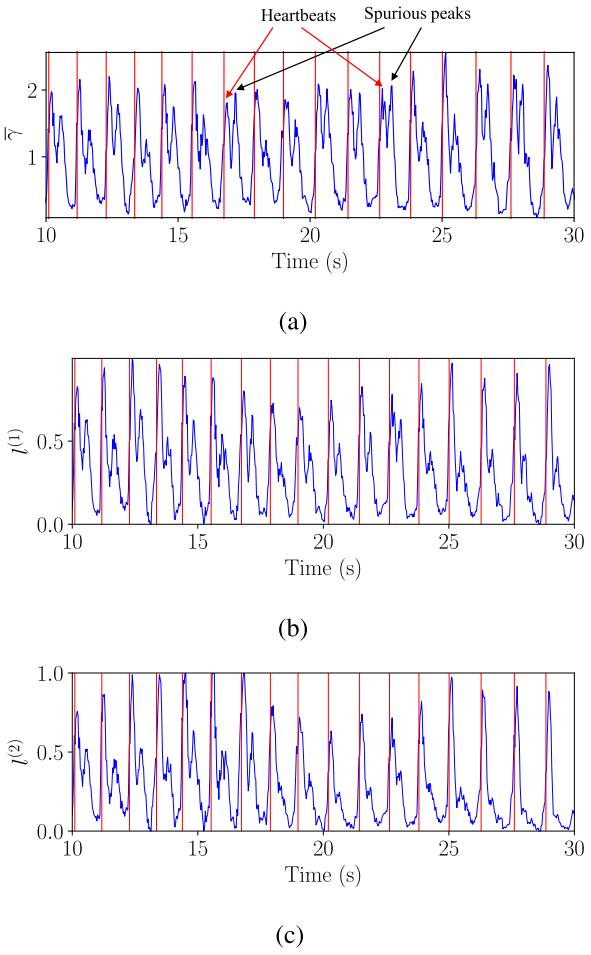

FIGURE 11. Representation of: a) a specific sequence $\{\overline{\gamma}[n]\}$; b) the corresponding sequence $\{l^{(1)}[n]\}$ generated by a single use of the proposed equalization-normalization procedure; c) the sequence $\{l^{(2)}[n]\}$ resulting from the application of equalization-normalization procedure to $\{l^{(1)}[n]\}$. In all the subfigures, vertical red lines are drawn to indicate the timing of the cardiac events detected by the employed ground truth sensor.

This concludes our description of the PHYHRVE; its steps are summarized in Algorithm 1 (note the dependence of various sequences and quantities on the iteration index t of the equalization-normalization procedure). This algorithm deserves various relevant comments, which are listed below.

On the use of the second derivative - The use of the first derivative of the unwrapped phase (see (16)) to enhance its cardiac component with respect to the respiratory one has been proposed in [33]. Since phase variations are directly proportional to displacement (i.e., range) variations (see (10)), the computation of the first derivative produces a *velocity signal*. The first derivative is also employed in [34] for the same purpose; here, this operation is followed by a couple of filtering stages and, in particular, by a band-pass filter selecting the spectral components that belong to the cardiac frequency region and by a bank of notch filters canceling the spectral contribution of respiratory harmonics falling in that region. The main disadvantage of this approach is represented by the fact that the cardiac component could be also canceled if it overlaps with a breath harmonic or if the respiratory frequency is incorrectly estimated [18], [35]. A better alternative to the first derivative is represented by the second derivative of the phase signal (see (14)), that can be seen as an *acceleration signal*. The computation of the second derivative has been shown to emphasize sharp variations due to individual heartbeats, while attenuating slow respiratory movements [36], [37], [38].

On selection combining and the generation of a single sequence for HRV estimation - Our EHS selection strategy is based on the fact that the best EHSs (i.e., those containing the strongest cardiac components) are highly correlated. Conversely, those containing the contribution of significant RBMs or lacking relevant cardiac information are poorly correlated. This has motivated the selection of the $\hat{L}$ EHSs exhibiting the highest sum of covariances (see (19)). Note also that the $\hat{L}$ sequences $\{\{\hat{\phi}_i''[n]\}; i = 1, 2, \ldots, \hat{L}\}$ are not guaranteed to be perfectly aligned during the fast oscillations induced by heart activity; however, they are expected not to have opposite signs because of the adopted selection algorithm (that aims at choosing the sequences that exhibit the highest correlation); consequently, the *envelope* of $\{\psi[n]\}$ is expected to strengthen in correspondence of the vibrations induced by heartbeats; this envelope is extracted by computing $\{\gamma[n]\}$ (see (24)).

Algorithm 1 PHYsiology-Inspired Heart Rate Variability Estimation (PHYHRVE) Algorithm

Input: $\{\tilde{\phi}_l[n]\}$ (13), $\{\sigma^{(t)}; t = 1, 2, .., T\}$, $\hat{L}$, M, $i_{\min}$, $i_{\max}$, T and S.
Begin:
Compute $\{\tilde{\phi}_l''[n]\}$ according to (14).
Compute $W_{l,j}$ according to (17).
Evaluate Q_l (see (19)).
Compute $\{\psi[n]\}$ on the basis of (21).
Evaluate $\{\xi[n]\}$ according to (23).
Compute $\{\gamma[n]\}$ according to (24).
Evaluate $\hat{f}_{\mathrm{h}}$ according to (26).
Compute $\{\bar{\gamma}[n]\}$ (28).
for $t = 1, 2, \ldots, T$ **do**
    Evaluate $\{G^{(t)}[n]\}$ on the basis of (30).
    Generate $\{\alpha^{(t)}[n]\}$ according to (29).
    Evaluate $\alpha_{\min}^{(t)}$ (35) and $\alpha_{\max}^{(t)}$ (36).
    Compute $\{l^{(t)}[n]\}$ according to (34).
end for
Output: $\{\hat{l}[n]\}$

IV. NUMERICAL RESULTS

The aim of this section is threefold. First, the technical specifications of the employed sensors and the developed measurement setup are described. Then, we focus on the extraction of cardiac peaks from the sequence

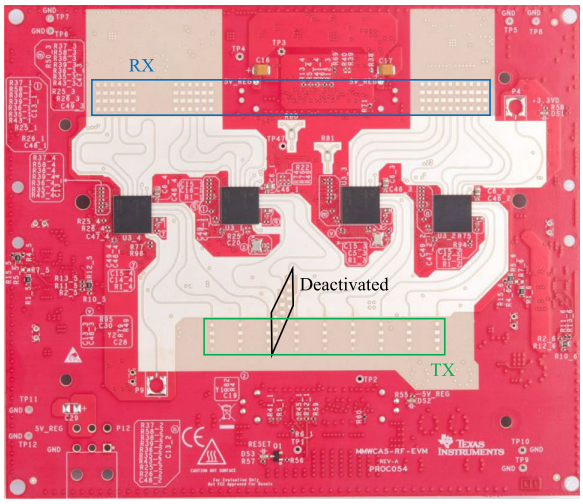

FIGURE 12. Front end of the TIDEP-01012 Cascade mmWave radar [39]; its planar TX and RX arrays are delimited by green and blue rectangles, respectively.

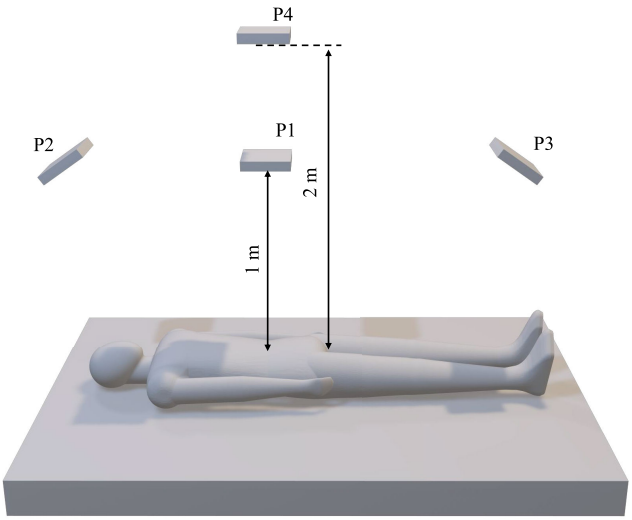

FIGURE 13. The considered measurement setup: the radar is positioned 1 m above the chest (P1), 1 m above the head (P2), 1 m above the feet (P3) and 2 m above the chest (P4).

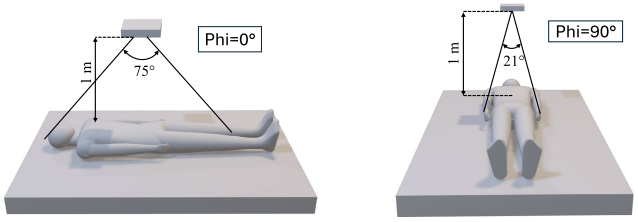

FIGURE 14. Representation of the radar orientation: 75° (Phi = 0° plane) and 21° (Phi = 90° plane) beamwidths illuminate the length and width, respectively, of the monitored subject's body.

$\{\hat{l}[n]\}$ generated by the equalization-normalization procedure described in the previous section. Finally, some metrics for quantifying HRV are defined and their values are evaluated on the basis of our experimental results.

A. EXPERIMENTAL SETUP

Our measurements have been acquired through the FMCW TIDEP-01012 *Cascade mmWave radar*, manufactured by Texas Instruments Inc. [39]. In our work, the following parameters have been selected for this radar device: a) chirp slope $\mu = 87$ MHz/μ s; b) central frequency $f_c = 77$ GHz; c) sampling frequency $f_s = 1/T_s = 10$ MHz; d) number of samples per chirp $N = 512$; e) chirp duration $T = 51$ μ s; f) frame period $T_F = 30$ ms. It is important to keep in mind that the front end of our radar device is equipped with a planar array composed of $N_T = 12$ TX antennas and $N_R = 16$ RX antennas (see Fig. 12). Consequently, in principle, $12 \times 16 = 192$ VAs are available. However, in practice, only a portion of the available virtual array is exploited; the selected portion consists of 86 distinct virtual elements forming a ULA (the distance between adjacent virtual elements is $d = \lambda/4$).

The wearable *Shimmer3 ECG Unit* device [40] has also been used as a reference sensor, since it makes accurate estimation of vital signs possible. This FDA-approved device, manufactured by Shimmer Research Ltd, is equipped with: a) a Bluetooth radio interface for the transmission of the acquired measurements; b) five electrodes, which need to be placed in specific positions on the chest of the subject under test [40]. In our acquisitions, the reference ECG signal has been read from the voltage difference between the left leg and RHS midaxillary (LL-RA) electrodes at a frequency equal to 256 Hz.[8] The time-domain signal sent through the Bluetooth interface has been processed by the Pan-Tompkins algorithm [41], followed by peak selection for the accurate estimation of cardiac R peaks. Thanks to the availability of a proper API, Shimmer3 measurements can be easily synchronized in time with those acquired through the employed radar device, so that data acquisition can be accomplished in real-time. In fact, the Shimmer3 device can share its time reference (namely, its CPU timestamp) with the radar device; this has allowed us to synchronize the reference sensor and the radar with high accuracy.

In our work, a *baseline* measurement of HRV has been performed [1]. This task, representing the first measurement step in HRV experiments (and usually followed by a *reactivity* and *recovery* step), involves the frontal monitoring of a single subject lying in a supine position, as shown in Fig. 13; the subject is asked not to talk or move, to relax, and to breathe spontaneously[9] [1]. In our experiments, the radar has been installed in front of the monitored subject. As shown in Fig. 13, in order to assess the accuracy of the proposed method in different scenarios, four different

[8] According to [2], a sampling rate of at least 200 Hz should be employed to achieve good accuracy in HR estimation.

[9] Our measurement scenario is consistent with that described in other publications on radar-based HRV estimation [11], [36], [42] or ECG [43], [44].

positions (denoted Px, with x=1, 2, 3 and 4) have been considered for the employed radar device [45], [46]: 1) placed above the chest (P1), above the head (P2) and above the feet (P3), in all cases at approximately 1 m from the body; 2) placed above the chest at approximately 2 m from the body (P4).

The radar employed in our study has FOVs of 75° and 21° (3dB beamwidth) in the Phi = 0° and Phi = 90° planes, respectively [47]; as illustrated in Fig. 14, in our experiments, we consistently oriented the radar in a way that the wider beamwidth illuminated the length of the monitored subject, whereas the narrower beamwidth illuminated his/her width. Our experimental results have evidenced that:

1) regardless of the radar position and distance, the best accuracy in IBI estimation is achieved when the chest falls within the FOV. For this reason, the numerical results discussed in the following (see Subsection IV-B) have been obtained using the radar positions represented in Fig. 13 while ensuring that the patient's chest fall within the FOV.

2) If the orientation shown in Fig. 14 is adopted for the radar device, its ULA is aligned parallel to the longitudinal axis of the body and its MIMO capabilities are fully exploited. In this configuration, different azimuthal angles correspond to distinct points along the vertical axis of the body.

Our measurements, each lasting 60 s,[10] have been acquired from four volunteers; three distinct measurements have been acquired for each of the positions shown in Fig. 13. Moreover, each subject has been given a few minutes before starting the acquisitions from him/her so that he/she could adapt to the measurement environment [49]. The overall duration of the measurements acquired from all the volunteers is 1920 s.

B. ASSESSMENT OF HEART RATE VARIABILITY

The values of the parameters we selected for the PHYHRVE are listed in Table 1. It is important to point out that:

a) In our experiments, $L = 100$ measurements have been acquired through the available virtual array; distinct measurements correspond to different points of the monitored body. The availability of a large number of measurements plays an important role since, due to the randomness of the position of the monitored subject and his/her possible RBMs, the presence of cardiac vibrations might be well detectable in a limited number of points of his/her body.

b) Few (in practice, $\hat{L} = 5$) measurements have been selected in the large set of available ones. On the one hand, increasing $\hat{L}$ results in a better exploitation of the available spatial diversity. On the other hand, this may introduce a number of spurious peaks caused by RBMs or noise. In addition, since cardiac vibrations propagate with a *finite speed* within the tissues and the cardiovascular system [27], a large value of $\hat{L}$ may lead to combining measurements characterized by significantly different *time lags*; this might result in a destructive combination of the EHS (see (21)). Our experimental results have evidenced that the choice $\hat{L} = 5$ represents a good trade-off.

c) The choice $M = 6$ has been made for the second filtering stage on the basis of a trial-and-error procedure.

d) The choices $i_{\min} = 10$ and $i_{\max} = 40$ have been made on the basis of (31) and (32), respectively, given $T_F = 30$ ms.

e) The standard deviations $\sigma^{(1)} = 2$ and $\sigma^{(2)} = 1$ have been selected for the first iteration and the second one, respectively, of the amplitude equalization algorithm. This choice results in an effective suppression of spurious peaks.

A detailed derivation of the computational complexity of the PHYHRVE is illustrated in Appendix A. The orders of the computational complexity of the PHYHRVE and related methods, such as mmHRV [3] and Pi-ViMo [27], are listed in Table 2; in particular, the provided expressions refer to the overall number of flops required for processing the measurements that are acquired over N_F consecutive frames. The content of Table 2 deserves the following comments:

a) The contributions of the 2D *Constant False Alarm Rate* (CFAR) and *Variational Mode Decomposition* (VMD) algorithms to the computational complexity of the mmHRV method are represented by the term $N_0\, N_1\, N_{rx}\, N_{ry}$ and the factor IK multiplying the FFT order $N_0' \log_2 N_0'$, respectively; here, the parameters N_{rx} and N_{ry} define the size of the reference window used by the 2D CFAR, whereas I and K represent the number of VMD iterations and the number of components generated by the decomposition, respectively.

b) Unlike the PHYHRVE and mmHRV methods, the Pi-ViMo technique does not employ beamforming; for this reason, the term $(N_0 N_1 \log_2 N_1) N_F$, that appears in the orders of the other two methods, is missing. Moreover, it uses a 1D CFAR, whose complexity is lower (by a factor of N_{ry}) than that required by the mmHRV method for the same task. Keep in mind, however, that the Pi-ViMo method computes the FFT for each target identified by the CFAR; this results in the presence of the additional term $(N-1)N_0' \log_2 N_0'$ with respect to the PHYHRVE method. Furthermore, the mmHRV method employs a coherent combining strategy, whose contribution is represented by the N_{MSP}^2 term, where N_{MSP} represents the total number of range bins selected by the *multi-point scattering* (MSP) algorithm.

These considerations explain why the PHYHRVE method, that does not make use of the CFAR or VMD algorithms, has a lower computational complexity than that of the mmHRV and Pi-ViMo methods when N_F is sufficiently small, (say, $N_F < 50$). However, if longer acquisitions or higher frame rates are considered, the computational gap reduces because of the increase of the term N_F^2 that appears in the computational complexity of the PHYHRVE method.

In the implementation of the PHYHRVE, the findpeaks function of Matlab R2022b has been employed to identify the position of the peaks[11] contained in the sequence $\{\hat{l}[n]\}$

[10] The validity of ultra-short-term HRV measurements (< 5 min) has been illustrated in [44] and [48].

[11] An alternative search strategy based the *constant false alarm rate* algorithm [50] could be employed; this would provide similar results.

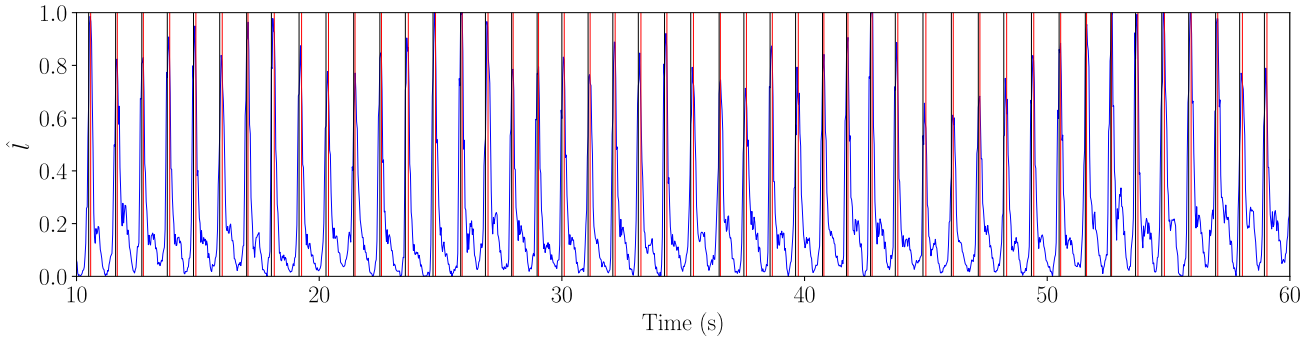

FIGURE 15. Representation of the sequence $\{\hat{l}[n]\}$, the positions of the peaks detected by the findpeaks function (black vertical lines) and the positions of the cardiac beats detected by our reference sensor (red vertical lines).

TABLE 1. Parameters adopted for the PHYHRVE.

Parameter	Meaning	Selected value
L	Number of available phase signals	100
$\hat{L}$	Number of selected phase signals	5
M	Window size of the second filter	6
f_{cut}	Cut-off frequency of the filter for compensating for amplitude variability	$\hat{f}_{\text{h}}/2$
$i_{\min}$	Minimum value of the indices (p, q) in (30)	10
$i_{\max}$	Maximum value of the indices (p, q) in (30)	40
$\{\sigma^{(1)}, \sigma^{(2)}\}$	Sequence of standard deviations	$\{2, 1\}$
S	Normalization depth	$4T_{\text{F}}/\hat{f}_{\text{h}}$
T	Number of iterations accomplished in the equalization-normalization procedure	2

TABLE 2. Order of the computational complexity characterizing the PHYHRVE, mmHRV and Pi-ViMo methods.

Algorithm	$\mathcal{O}(\cdot)$
mmHRV [3]	$\mathcal{O}([N_0(N_{\text{V}} \log_2 N_0 + N_1(\log_2 N_1 + N_{\text{rx}}N_{\text{ry}})) + N^2]N_{\text{F}} + IKN_0' \log_2 N_0')$
Pi-ViMo [27]	$\mathcal{O}(N_0(N_{\text{V}} \log_2 N_0 + N_{\text{rx}})N_{\text{F}} + N_0'(N \log_2 N_0'^2 + N_{\text{MSP}}^2))$
PHYHRVE	$\mathcal{O}([N_0(N_{\text{V}} \log_2 N_0 + N_1 \log_2 N_1) + L^2 + N_{\text{F}}]N_{\text{F}} + N_0' \log_2 N_0')$

(available at the output of the equalization-normalization stage of our algorithm). Note that the mean HR estimate $\hat{f}_{\text{h}}$ can be employed to set the MinPeakDistance parameter of this function in order to limit the minimum peak distance at $((\hat{f}_{\text{h}} + \delta)T_{\text{F}})^{-1}$; here, δ is the expected maximum HRV during the acquisition in Hz. The output of this function is the H-dimensional vector

$$\hat{h} = \left[\hat{h}[1], \hat{h}[2], \ldots, \hat{h}[H]\right], \tag{37}$$

collecting the indices of the elements of $\{\hat{l}[n]\}$ associated with the H detected peaks. Note that the size H of $\hat{h}$ increases with the acquisition duration and the average HR. An example of the results generated by the PHYHRVE is shown in Fig. 15, in which the sequence $\{\hat{l}[n]\}$, the positions of the peaks detected by the employed function, and the positions of the cardiac beats detected by our reference sensor are shown. In this case, the instants of the detected peaks almost perfectly coincide with those of the ground truth beats.

Given the vector $\hat{h}$ (37), the $(H-1)$-dimensional vector $\hat{T}_{\text{IBI}}$ collecting the associated IBIs can be easily generated;

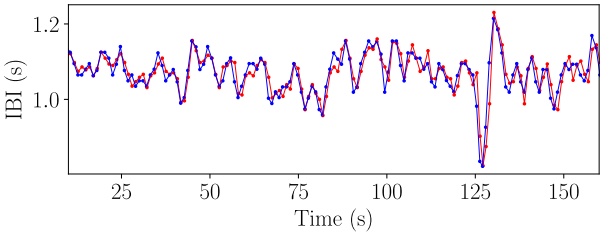

FIGURE 16. Representation of our radar-based estimates of IBI (red curve) and of the ground truth values obtained through our reference sensor (blue curve); a linear interpolation is used to ease reading.

the nth element of the last vector is defined as

$$\hat{T}_{\text{IBI}}[n] \triangleq \left(\hat{h}[n+1] - \hat{h}[n]\right) T_{\text{F}}, \tag{38}$$

with $n = 1, 2, \ldots, H-1$. Some numerical results are offered in Fig. 16, where the radar-based estimates of IBIs evaluated by our algorithm and the associated ground truth values obtained through our reference sensor are represented (an observation interval lasting 180 s is considered). The corresponding values of HR are represented in Fig. 17.

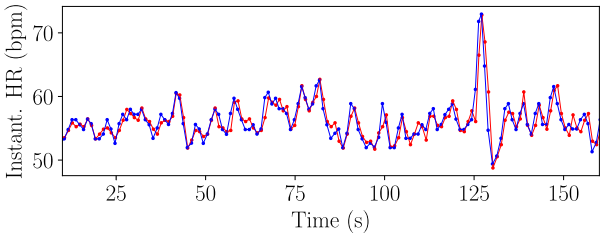

FIGURE 17. Representation of our radar-based estimates of HR (red curve) and of the ground truth values obtained through our reference sensor (blue curve); a linear interpolation is used to ease reading.

Ultra-short-term variations in HR (i.e., the variations observed over an interval having duration $\sim$ 5 min [48]) can be assessed in different ways. The simplest one is based on the acquisition of *time domain measures* [2]. In this case, both the instantaneous HR and the intervals between normal QRS complexes[12] are evaluated. In a continuous ECG trace, each QRS complex is detected, and the *normal-to-normal intervals* (NNs) or the instantaneous HR are determined. In this work, all the observed R peaks are assumed to be normal, so that NNs are identical to the R peak-R peak intervals. Given the NNs, the simplest parameter quantifying HRV is the *standard deviation of the NN intervals* (SDNN); note that, in the absence of abnormal R peaks, the SDNN is equivalent to the *standard deviation of R peak-R peak intervals* (SDRR) [48]. The SDNN accounts for the contributions due to all cyclic components that are responsible for the variability observed in the recording period. Another parameter involving the difference between intervals is *the square root of the mean squared differences of successive NN intervals* (RMSSD). All these parameters, being obtained from ultra-short-term variation measurements, estimate high-frequency HR variations and, therefore, are highly correlated [2].

The aforementioned metrics have been evaluated on the basis of the entire available dataset, collecting both radar and ECG measurements. Our main results, for each individual and radar position, are listed in Table 3. From these results it can be inferred that:

a) an appreciable accuracy is achieved, in terms of both SDNN and RMSSD, for every radar position; in fact, our results are either aligned with or even better than those provided in related works [9], [22], [36].

b) The largest SDNN has been measured for subject 3 in P4; note also that, in general, slightly worse performance been obtained for P4.

[12]The QRS complex represents the electrical activity of the ventricles and is the most recognizable waveform indicating heart activity. The QRS complex is composed by an initial downward spike, an upward spike, and a second downward spike (these are called Q wave, R wave and S wave, respectively) [51], [52]. In this context, normal QRS complexes are defined as those resulting from the depolarization of the sinoatrial node and, therefore, not caused by artifacts or defective sensors.

TABLE 3. Numerical results based on the time domain measurements of HRV computed over the whole dataset.

Radar location	Subject No.	HRV metric	u.m.	Sensor type: Shimmer 3 ECG	Sensor type: **Radar**	deviation
P1	#1	**SDNN**	ms	45.41	42.99	5.32%
		RMSSD	ms	43.15	37.28	13.6%
	#2	**SDNN**	ms	50.06	50.19	0.26%
		RMSSD	ms	34.10	37.48	9.92%
	#3	**SDNN**	ms	48.55	45.75	5.78%
		RMSSD	ms	44.32	45.75	3.23%
	#4	**SDNN**	ms	54.69	55.40	1.30%
		RMSSD	ms	40.75	39.10	4.03%
P2	#1	**SDNN**	ms	86.63	90.80	4.82%
		RMSSD	ms	54.83	51.75	5.62%
	#2	**SDNN**	ms	47.72	44.59	6.57%
		RMSSD	ms	31.36	30.27	3.49%
	#3	**SDNN**	ms	44.83	48.01	7.1%
		RMSSD	ms	39.35	34.67	11.89%
	#4	**SDNN**	ms	46.14	43.22	6.34%
		RMSSD	ms	24.89	27.39	10.04%
P3	#1	**SDNN**	ms	49.88	48.26	3.25%
		RMSSD	ms	32.01	27.27	14.83%
	#2	**SDNN**	ms	59.47	59.48	0.01%
		RMSSD	ms	30.28	31.40	3.71%
	#3	**SDNN**	ms	41.06	41.42	0.89%
		RMSSD	ms	32.80	28.96	11.71%
	#4	**SDNN**	ms	72.89	71.01	2.58%
		RMSSD	ms	20.38	25.38	24.53%
P4	#1	**SDNN**	ms	60.89	64.26	5.53%
		RMSSD	ms	52.24	55.31	5.87%
	#2	**SDNN**	ms	58.57	61.14	4.39%
		RMSSD	ms	42.21	51.45	21.90%
	#3	**SDNN**	ms	47.78	52.19	9.22%
		RMSSD	ms	48.00	47.86	0.30%
	#4	**SDNN**	ms	46.18	44.91	2.74%
		RMSSD	ms	36.26	33.87	6.59%

c) The overall performance in terms of RMSSD looks poorer than that expressed in terms of SDNN; deviations larger than 20 % have been obtained only for P3 and P4.

Based on our experimental results, we can state that the measurement setups characterized by the radar positioned at 1 m above the chest and head (P1 and P2) are the best ones. This can be explained as follows. In P4, a lower SNR is obtained beacuse of the greater distance between the radar and the subject. In P3, instead, although the radar height is optimal, the vibrations caused by cardiac activity are less observable than in P2.

Bland-Altman Limits of Agreement methods can be employed to analyse ultra-short-term HRV measurements [48], [53]. The Bland-Altman plot, obtained on the basis of our data acquired for P1,[13] is illustrated in Fig. 18.

[13]We decided to generate the Bland-Altman plot for this position only, as including all the available data would have reduced the intelligibility of the plot.

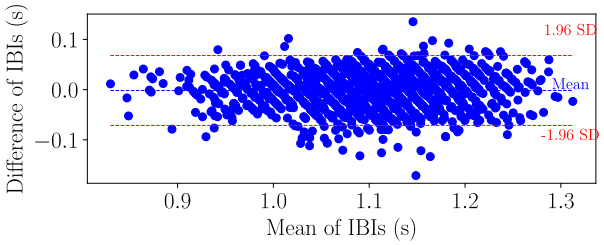

FIGURE 18. Bland-Altman plot of IBI measurements; only those originated from P1 radar position have been employed.

Since the dashed blue horizontal line, which indicates the mean differences between the ECG-based IBI and the IBI computed by the PHYHRVE, is positioned at -0.0025 s, there is no relevant bias. Moreover, the dashed red horizontal lines, positioned at 0.0799 s and -0.0849 s, and delimiting the 95% confidence intervals, evidence that the differences between the ECG-based IBI and the IBI computed by the PHYHRVE algorithm are usually small. In conclusion, our results show a satisfactory agreement between the IBIs measured by the two employed sensors, so confirming the reliability of the proposed method.

V. CONCLUSION

In this manuscript, a new method for HRV estimation, called PHYHRVE, has been illustrated. It is able to estimate the intervals separating consecutive cardiac peaks on the basis of the unwrapped phase extracted from the measurements that originate from multiple points of the body of the monitored subject. Various experimental results, based on the measurements provided by a MIMO FMCW radar operating at 77 GHz and acquired from four different subjects, have been illustrated. Such results evidence that: a) the accuracy achieved by our algorithm, in terms of time domain metrics such as SDNN and RMSSD, is similar to that offered by an ECG; b) good performance is obtained when the radar is positioned 1 m above the head or above the chest of the monitored subject. Our ongoing research activities aim at assessing the performance on a larger group of healthy adult volunteers and at improving the strategy adopted to select and combine multiple measurements in a single signal conveying cardiac information.

APPENDIX A
COMPUTATIONAL COMPLEXITY

In this appendix, the computational complexity, in terms of *floating-point operations* (flops), of the PHYHRVE algorithm described in Sections II-III is derived. To begin, it is useful to note that computational complexity $\mathcal{C}_{\text{PHYHRVE}}$ can be expressed as

$$\mathcal{C}_{\text{PHYHRVE}} \triangleq \mathcal{C}^{(\text{pre})}_{\text{PHYHRVE}} + \mathcal{C}^{(\text{main})}_{\text{PHYHRVE}}, \tag{39}$$

where:

a) $\mathcal{C}^{(\text{pre})}_{\text{PHYHRVE}}$ represents the cost of the *pre-processing steps* described in Section II; these include the computation of the AP and the phase extraction followed by unwrapping for the L AP bins whose coordinates are contained in the set $\{(p_l, q_l);\, l = 1, 2, \ldots, L\}$.

b) $\mathcal{C}^{(\text{main})}_{\text{PHYHRVE}}$ represents the cost of the *main processing steps* described in Section III.

The general criteria adopted in assessing $\mathcal{C}^{(\text{pre})}_{\text{PHYHRVE}}$ and $\mathcal{C}^{(\text{main})}_{\text{PHYHRVE}}$ are the same as those illustrated in [54] and can be summarised as follows:

- $2d$ flops are required to compute the element-wise sum $\mathbf{u}_c + \mathbf{v}_c$ of two d-dimensional complex vectors;
- $6d$ flops are required to compute the element-wise product $\mathbf{u}_c \cdot \mathbf{v}_c$ of two d-dimensional complex vectors;
- d flops are required to find the maximum element of a vector $\mathbf{v} \in \mathbb{R}^d$;
- $d \log_2 d$ flops are required to compute an order d FFT.

According to these criteria, the computational cost $\mathcal{C}^{(\text{pre})}_{\text{PHYHRVE}}$, for a single acquisition involving N_{F} consecutive frames, is evaluated as

$$\mathcal{C}^{(\text{pre})}_{\text{PHYHRVE}} = \left(\mathcal{C}_y + \mathcal{C}_{\tilde{\phi}}\right) N_{\text{F}} \tag{40}$$

where:

a) $\mathcal{C}_y = N_0(N_{\text{V}} \log_2 N_0 + N_1 \log_2 N_1)$ is the contribution due to the computation of the sequence $\{y^{(n)}[p, q]\}$ (11), and;

b) $\mathcal{C}_{\tilde{\phi}} = 4L$ is the contribution due to the computation of the set of unwrapped phase sequences $\{\{\tilde{\phi}_l[n]\};\, l = 1, 2, .., L\}$ (12)-(13).

The cost $\mathcal{C}^{(\text{main})}_{\text{PHYHRVE}}$, instead, is evaluated as

$$\begin{aligned}\mathcal{C}^{(\text{main})}_{\text{PHYHRVE}} &= \mathcal{C}_{\tilde{\phi}''} + \mathcal{C}_{\text{sel}} + \mathcal{C}_{\psi} + \mathcal{C}_{\gamma} + \mathcal{C}_{\bar{\text{HR}}} + \mathcal{C}_{\bar{\gamma}} + T(\mathcal{C}_{\alpha} + \mathcal{C}_{l})\end{aligned} \tag{41}$$

where:

a) $\mathcal{C}_{\tilde{\phi}''} = L(2N_{\text{F}} - 3)$ is the contribution due to the computation of $\{\tilde{\phi}_l{}''\}$ on the basis of (14).

b) $\mathcal{C}_{\text{sel}} = \mathcal{C}_Q + \mathcal{C}_W + \mathcal{C}_{\eta}$ is the contribution due to the selection step; here, $\mathcal{C}_Q = L(L-1)$ is the contribution due to the computation of $\{Q_l\}$ (19), $\mathcal{C}_W = L(L-1)[4(N_{\text{F}} - 2) - 1]$ is the contribution due to the computation of $\{W_{l,j}\}$ (17) and $\mathcal{C}_{\eta} = L(N_{\text{F}} - 2)$ is the contribution due to the computation of $\{\eta_{\tilde{\phi}''}[n]\}$ (18).

c) $\mathcal{C}_{\psi} = 2\hat{L}$ is the contribution due to the computation of $\{\psi[n]\}$ (21).

d) $\mathcal{C}_{\gamma} = M(M-1)(N_{\text{F}} - 2)$ is the overall contribution due to the computation of $\{\gamma[n]\}$ (24).

e) $\mathcal{C}_{\bar{\text{HR}}} = N_0' \log_2 N_0' + h_{\max} - h_{\min}$ is the overall contribution due to the computation of $\hat{f}_{\text{h}}$ (26).

f) $\mathcal{C}_{\bar{\gamma}} = 9(N_{\text{F}} - 2)$ is the overall contribution due to the computation of $\{\bar{\gamma}[n]\}$ (28).

g) $\mathcal{C}_{\alpha} = 3(i_{\max} - i_{\min})^2$ is the overall contribution due to the computation of $\{\alpha[n]\}$ (29).

h) $\mathcal{C}_{l} = 2N_{\text{F}}(N_{\text{F}} - M - 4 - 2i_{\max}) + 2$ is the overall contribution due to the computation of $\{l[n]\}$ (34).

Based on the last mathematical results, the overall complexity of the PHYHRVE can be expressed as

$$\begin{aligned}\mathcal{C}_{\text{PHYHRVE}} &= \left[N_0\left(N_{\text{V}}\log_2 N_0 + N_1\log_2 N_1\right)\right. \\ &\quad + (4L+3)\,L + 2N_{\text{F}} + M(M-3) - 4i_{\max} + 1\left.\right]N_{\text{F}} \\ &\quad + (-8L+4)\,L + 2\hat{L} - 2M\,(M-1) + N_0'\log_2 N_0' \\ &\quad + 3\,(i_{\max} - i_{\min})^2 + h_{\max} - h_{\min} - 18 \qquad (42)\end{aligned}$$

Dropping the least relevant terms in the last formula leads to the PHYHRVE complexity order provided in Table 2.

REFERENCES

[1] S. Laborde, E. Mosley, and J. F. Thayer, "Heart rate variability and cardiac vagal tone in psychophysiological research – recommendations for experiment planning, data analysis, and data reporting," *Frontiers Psychol.*, vol. 8, Feb. 2017, Art. no. 238557.

[2] M. Malik, J. T. Bigger, A. J. Camm, R. E. Kleiger, A. Malliani, A. J. Moss, and P. J. Schwartz, "Heart rate variability: Standards of measurement, physiological interpretation, and clinical use," *Eur. Heart J.*, vol. 17, no. 3, Mar. 1996.

[3] F. Wang, X. Zeng, C. Wu, B. Wang, and K. J. R. Liu, "MmHRV: Contactless heart rate variability monitoring using millimeter-wave radio," *IEEE Internet Things J.*, vol. 8, no. 22, pp. 16623–16636, Nov. 2021.

[4] A. Gharamohammadi, A. Khajepour, and G. Shaker, "In-vehicle monitoring by radar: A review," *IEEE Sensors J.*, vol. 23, no. 21, pp. 25650–25672, 2023.

[5] Y. Zhang, R. Yang, Y. Yue, E. Gee Lim, and Z. Wang, "An overview of algorithms for contactless cardiac feature extraction from radar signals: Advances and challenges," *IEEE Trans. Instrum. Meas.*, vol. 72, pp. 1–20, 2023.

[6] S. Ji, Z. Zhang, Z. Xia, H. Wen, J. Zhu, and K. Zhao, "RBHHM: A novel remote cardiac cycle detection model based on heartbeat harmonics," *Biomed. Signal Process. Control*, vol. 78, Sep. 2022, Art. no. 103936.

[7] U. Ha, S. Assana, and F. Adib, "Contactless seismocardiography via deep learning radars," in *Proc. 26th Annu. Int. Conf. Mobile Comput. Netw.*, New York, NY, USA, Sep. 2020, pp. 1–14.

[8] K. Yamamoto, R. Hiromatsu, and T. Ohtsuki, "ECG signal reconstruction via Doppler sensor by hybrid deep learning model with CNN and LSTM," *IEEE Access*, vol. 8, pp. 130551–130560, 2020.

[9] J. N. Sameera, M. S. Ishrak, V. M. Lubecke, and O. Boric-Lubecke, "Enhancing beat-to-beat analysis of heart signals with respiration harmonics reduction through demodulation and template matching," *IEEE Trans. Microw. Theory Techn.*, vol. 72, no. 1, pp. 750–758, Jan. 2024.

[10] K. Yamamoto, K. Toyoda, and T. Ohtsuki, "Spectrogram-based non-contact RRI estimation by accurate peak detection algorithm," *IEEE Access*, vol. 6, pp. 60369–60379, 2018.

[11] C. Gouveia, D. F. Albuquerque, P. Pinho, and J. Vieira, "Bio-radar cardiac signal model used for HRV assessment and evaluation using adaptive filtering," *IEEE Trans. Instrum. Meas.*, vol. 71, pp. 1–10, 2022.

[12] M. Bouazizi, K. Yamamoto, K. Endo, and T. Ohtsuki, "A novel approach for heartbeat rate estimation using 3-D lidar and multibeam MIMO Doppler radar," *IEEE Sensors J.*, vol. 23, no. 24, pp. 31259–31277, 2023.

[13] J. N. Sameera, M. S. Ishrak, V. Lubecke, and O. Boric-Lubecke, "Effect of respiration harmonics on beat-to-beat analysis of heart signal," in *IEEE MTT-S Int. Microw. Symp. Dig.*, Jun. 2023, pp. 1081–1084.

[14] T. Ohtsuki and E. Mogi, "Heartbeat detection with Doppler radar based on estimation of average R-R interval using Viterbi algorithm," in *Proc. IEEE 27th Annu. Int. Symp. Pers., Indoor, Mobile Radio Commun. (PIMRC)*, Sep. 2016, pp. 1–5.

[15] W. Xia, Y. Li, and S. Dong, "Radar-based high-accuracy cardiac activity sensing," *IEEE Trans. Instrum. Meas.*, vol. 70, pp. 1–13, 2021.

[16] K. Yamamoto and T. Ohtsuki, "Noncontact heartbeat detection by Viterbi algorithm with fusion of beat-beat interval and deep learning-driven branch metrics," in *Proc. IEEE Int. Conf. Acoust., Speech Signal Process. (ICASSP)*, Jun. 2021, pp. 8308–8312.

[17] Q. Wu, Z. Mei, Z. Lai, D. Li, and D. Zhao, "A non-contact vital signs detection in a multi-channel 77GHz LFMCW radar system," *IEEE Access*, vol. 9, pp. 49614–49628, 2021.

[18] G. Paterniani, D. Sgreccia, A. Davoli, G. Guerzoni, P. Di Viesti, A. C. Valenti, M. Vitolo, G. M. Vitetta, and G. Boriani, "Radar-based monitoring of vital signs: A tutorial overview," *Proc. IEEE*, vol. 111, no. 3, pp. 277–317, Mar. 2023.

[19] S. M. Patole, M. Torlak, D. Wang, and M. Ali, "Automotive radars: A review of signal processing techniques," *IEEE Signal Process. Mag.*, vol. 34, no. 2, pp. 22–35, Mar. 2017.

[20] A. Davoli, G. Guerzoni, and G. M. Vitetta, "Machine learning and deep learning techniques for colocated MIMO radars: A tutorial overview," *IEEE Access*, vol. 9, pp. 33704–33755, 2021.

[21] B.-K. Park, O. Boric-Lubecke, and V. M. Lubecke, "Arctangent demodulation with DC offset compensation in quadrature Doppler radar receiver systems," *IEEE Trans. Microw. Theory Techn.*, vol. 55, no. 5, pp. 1073–1079, May 2007.

[22] H. Hu, Y. Chen, S. Li, J. Yang, and Z. Sun, "Seismocardiographic signals detection based on circulant singular spectrum analysis through millimeter wave radar," in *Proc. IEEE 6th Int. Conf. Signal Image Process. (ICSIP)*, Oct. 2021, pp. 720–724.

[23] O. T. Inan, P.-F. Migeotte, K.-S. Park, M. Etemadi, K. Tavakolian, R. Casanella, J. Zanetti, J. Tank, I. Funtova, G. K. Prisk, and M. Di Rienzo, "Ballistocardiography and seismocardiography: A review of recent advances," *IEEE J. Biomed. Health Informat.*, vol. 19, no. 4, pp. 1414–1427, Jul. 2015.

[24] Y. Rong, A. Dutta, A. Chiriyath, and D. W. Bliss, "Motion-tolerant non-contact heart-rate measurements from radar sensor fusion," *Sensors*, vol. 21, no. 5, p. 1774, Mar. 2021.

[25] X. Zhang, X. Yang, Y. Ding, Y. Wang, J. Zhou, and L. Zhang, "Contactless simultaneous breathing and heart rate detections in physical activity using IR-UWB radars," *Sensors*, vol. 21, no. 16, p. 5503, Aug. 2021.

[26] Q. Liu, H. Guo, J. Xu, H. Wang, A. Kageza, S. AlQarni, and S. Wu, "Non-contact non-invasive heart and respiration rates monitoring with MIMO radar sensing," in *Proc. IEEE Global Commun. Conf. (GLOBECOM)*, Dec. 2018, pp. 1–6.

[27] B. Zhang, B. Jiang, R. Zheng, X. Zhang, J. Li, and Q. Xu, "Pi-ViMo: Physiology-inspired robust vital sign monitoring using mmWave radars," *ACM Trans. Internet Things*, vol. 4, no. 2, pp. 1–27, May 2023.

[28] G. Shafiq and K. C. Veluvolu, "Multimodal chest surface motion data for respiratory and cardiovascular monitoring applications," *Sci. Data*, vol. 4, no. 1, pp. 1–12, Apr. 2017.

[29] F. Wang, X. Zeng, C. Wu, B. Wang, and K. J. R. Liu, "Driver vital signs monitoring using millimeter wave radio," *IEEE Internet Things J.*, vol. 9, no. 13, pp. 11283–11298, Jul. 2022.

[30] C. Will, K. Shi, S. Schellenberger, T. Steigleder, F. Michler, J. Fuchs, R. Weigel, C. Ostgathe, and A. Koelpin, "Radar-based heart sound detection," *Sci. Rep.*, vol. 8, no. 1, p. 11551, Jul. 2018.

[31] J. Selva, "ML estimation and detection of multiple frequencies through periodogram estimate refinement," *IEEE Signal Process. Lett.*, vol. 24, no. 3, pp. 249–253, Mar. 2017.

[32] W. T. Zar and H. M. Tun, "Non-contact heartbeat detection using Viterbi algorithm based on distribution of difference of two-adjacent RR intervals," in *Proc. 11th Int. Conf. Robot., Vis., Signal Prond Power Appl.* Cham, Switzerland: Springer, 2022, pp. 405–411.

[33] J. Wang, X. Wang, L. Chen, J. Huangfu, C. Li, and L. Ran, "Noncontact distance and amplitude-independent vibration measurement based on an extended DACM algorithm," *IEEE Trans. Instrum. Meas.*, vol. 63, no. 1, pp. 145–153, Jan. 2014.

[34] M. Xiang, W. Ren, W. Li, Z. Xue, and X. Jiang, "High-precision vital signs monitoring method using a FMCW millimeter-wave sensor," *Sensors*, vol. 22, no. 19, p. 7543, Oct. 2022.

[35] A. Ahmad, J. C. Roh, D. Wang, and A. Dubey, "Vital signs monitoring of multiple people using a FMCW millimeter-wave sensor," in *Proc. IEEE Radar Conf. (RadarConf)*, Apr. 2018, pp. 1450–1455.

[36] X. Han, Q. Zhai, N. Zhang, X. Zhang, L. He, M. Pan, B. Zhang, and T. Liu, "A real-time evaluation algorithm for noncontact heart rate variability monitoring," *Sensors*, vol. 23, no. 15, p. 6681, Jul. 2023.

[37] L. Liu, J. Zhang, Y. Qu, S. Zhang, and W. Xiao, "MmRH: Noncontact vital sign detection with an FMCW mm-wave radar," *IEEE Sensors J.*, vol. 23, no. 8, pp. 8856–8866, Apr. 2023.

[38] L. Zhao, R. Lyu, Q. Lin, A. Zhou, H. Zhang, H. Ma, J. Wang, C. Shao, and Y. Tang, "MmArrhythmia: Contactless arrhythmia detection via mmWave sensing," *Proc. ACM Interact., Mobile, Wearable Ubiquitous Technol.*, vol. 8, no. 1, pp. 1–25, Mar. 2024.

[39] Texas Instrum. (Jun. 2019). *Design Guide: TIDEP-01012; Imaging Radar Using Cascaded Mmwave Sensor Reference Design*. [Online]. Available: https://www.ti.com/lit/ug/tiduen5a/tiduen5a.pdf
[40] Shimmer. (2018). *Shimmer3 ECG Unit*. [Online]. Available: https://shimmersensing.com/wp-content/docs/support/documentation/ECG_User_Guide_Rev1.12.pdf
[41] J. Pan and W. J. Tompkins, "A real-time QRS detection algorithm," *IEEE Trans. Biomed. Eng.*, vol. BME-32, no. 3, pp. 230–236, Mar. 1985.
[42] C. Tang, Y. Dai, Z. Li, Y. Song, F. Liang, and T. Jin, "BERT: Accelerating vital signs measurement for bioradar with an efficient recursive technique," 2024, *arXiv:2404.13315*.
[43] U. Nussinovitch, K. P. Elishkevitz, K. Katz, M. Nussinovitch, S. Segev, B. Volovitz, and N. Nussinovitch, "Reliability of ultra-short ECG indices for heart rate variability," *Ann. Noninvasive Electrocardiol.*, vol. 16, no. 2, pp. 117–122, Apr. 2011.
[44] M. L. Munoz, A. van Roon, H. Riese, C. Thio, E. Oostenbroek, I. Westrik, E. J. C. de Geus, R. Gansevoort, J. Lefrandt, I. M. Nolte, and H. Snieder, "Validity of (ultra-)short recordings for heart rate variability measurements," *PLoS ONE*, vol. 10, no. 9, Sep. 2015, Art. no. e0138921.
[45] L. Ren, S. Nahar, A. E. Fathy, T. Phan, N. Tran, and O. Kilic, "Investigation of vital signs monitoring errors due to subject's orientation, clothing and distance from a SFCW radar," in *Proc. IEEE Int. Symp. Antennas Propag. (APSURSI)*, Jul. 2016, pp. 1171–1172.
[46] L. Hornig, B. Szmola, W. Pätzold, J. P. Vox, and K. I. Wolf, "Evaluation of lateral radar positioning for vital sign monitoring: An empirical study," *Sensors*, vol. 24, no. 11, p. 3548, May 2024.
[47] Texas Instrum. (Sep. 2019). *Awrx Cascaded Radar Rf Evaluation Module*. [Online]. Available: https://www.ti.com/document-viewer/lit/html/swru553
[48] F. Shaffer and J. P. Ginsberg, "An overview of heart rate variability metrics and norms," *Frontiers Public Health*, vol. 5, Sep. 2017, Art. no. 290215.
[49] N. Ghuman, P. Campbell, and W. B. White, "Role of ambulatory and home blood pressure recording in clinical practice," *Current Cardiol. Rep.*, vol. 11, no. 6, pp. 414–421, Nov. 2009.
[50] M. A. Richards, *Fundamentals of Radar Signal Processing*, vol. 1. New York, NY, USA: McGraw-Hill, 2005.
[51] J. R. Levick, *An Introduction to Cardiovascular Physiology*. London, U.K.: Butterworth, 2013.
[52] A. Subasi, *Practical Guide for Biomedical Signals Analysis Using Machine Learning Techniques: A MATLAB Based Approach*. New York, NY, USA: Academic, 2019.
[53] J. M. Bland and D. G. Altman, "Measuring agreement in method comparison studies," *Stat. Methods Med. Res.*, vol. 8, no. 2, pp. 135–160, Jun. 1999.
[54] G. H. Golub and C. F. Van Loan, *Matrix Computations*. Baltimore, MD, USA: JHU press, 2013.

ELIA VIGNOLI (Graduate Student Member, IEEE) received the bachelor's and master's degrees (cum laude) in electronics engineering from the University of Modena and Reggio Emilia, in 2020 and 2022, respectively, where he is currently pursuing the Ph.D. degree in information and communication technologies. His main research interests include mm-wave radars for vital signs monitoring, with a particular emphasis on the development of new detection and estimation algorithms.

GIORGIO GUERZONI received the B.S. and M.S. degrees (cum laude) in electronics engineering and the Ph.D. degree in information and communication technologies from the University of Modena and Reggio Emilia, Italy, in 2019 and 2023, respectively. His research interests include signal processing and machine learning methods for MIMO radars.

GIORGIO MATTEO VITETTA (Senior Member, IEEE) received the Dr.Ing. (cum laude) and Ph.D. degrees in electronic engineering from the University of Pisa, Italy, in 1990 and 1994, respectively. He has been a Full Professor of telecommunications with the University of Modena and Reggio Emilia, since 2001. He has co-authored more than 100 articles published in international journals and on the proceedings of international conferences. He has co-authored the book *Wireless Communications: Algorithmic Techniques* (John Wiley), in 2013. His main research interests include wireless and wired data communications, localization systems, MIMO radars, and smart grids. He has served as an Area Editor for IEEE TRANSACTIONS ON COMMUNICATIONS and as an Associate Editor for IEEE WIRELESS COMMUNICATIONS LETTERS and IEEE TRANSACTIONS ON WIRELESS COMMUNICATIONS.